Published online: August 31, 2015

Article

SOURCE DATA | TRANSPARENT PROCESS | OPEN ACCESS

molecular systems biology

Stress-response balance drives the evolution of a network module and its host genome

Caleb González[1,†], Joe Christian J Ray[1,2,†], Michael Manhart[3,4], Rhys M Adams[1], Dmitry Nevozhay[1,5], Alexandre V Morozov[3,6] & Gábor Balázsi[1,7,8,*]

Abstract

Stress response genes and their regulators form networks that underlie drug resistance. These networks often have an inherent tradeoff: their expression is costly in the absence of stress, but beneficial in stress. They can quickly emerge in the genomes of infectious microbes and cancer cells, protecting them from treatment. Yet, the evolution of stress resistance networks is not well understood. Here, we use a two-component synthetic gene circuit integrated into the budding yeast genome to model experimentally the adaptation of a stress response module and its host genome in three different scenarios. In agreement with computational predictions, we find that: (i) intra-module mutations target and eliminate the module if it confers only cost without any benefit to the cell; (ii) intra- and extra-module mutations jointly activate the module if it is potentially beneficial and confers no cost; and (iii) a few specific mutations repeatedly fine-tune the module's noisy response if it has excessive costs and/or insufficient benefits. Overall, these findings reveal how the timing and mechanisms of stress response network evolution depend on the environment.

Keywords drug resistance; experimental evolution; positive feedback; synthetic gene circuit; tradeoff

Subject Categories Quantitative Biology & Dynamical Systems; Synthetic Biology & Biotechnology; Evolution

DOI 10.15252/msb.20156185 | Received 21 March 2015 | Revised 31 July 2015 | Accepted 4 June 2015

Mol Syst Biol. (2015) 11: 827

Introduction

The number of human-designed biological systems has increased rapidly since the inception of synthetic biology (Purnick & Weiss, 2009). Parts and concepts underlying synthetic biological constructs have expanded quickly, feeding on general biological knowledge. Conversely, synthetic biology has enormous but unexploited potential to inform other areas of biology, such as evolutionary biology (Tanouchi *et al*, 2012b).

For example, gene regulatory networks that control the expression of stress-protective genes have emerged through evolution (Lopez-Maury *et al*, 2008) but can also be built *de novo* (Nevozhay *et al*, 2012; Tanouchi *et al*, 2012a). Depending on the details of gene regulation, cells can survive because they respond to stress (Gasch *et al*, 2000); diversify non-genetically (hedge bets), independent of the stress (Balaban *et al*, 2004; Thattai & van Oudenaarden, 2004; Levy *et al*, 2012); or use a mixture of these two strategies (New *et al*, 2014). However, stress-protective gene expression can be costly or toxic in the absence of stress (Andersson & Levin, 1999), or even in the presence of stress when the expression level exceeds the requirement for survival (Nevozhay *et al*, 2012). Overall, the costs and benefits of survival mechanisms create a tradeoff between maximizing growth while also ensuring survival during stress. How mutations alter stress response networks to improve fitness under such circumstances, especially in phenotypically heterogeneous populations (Sumner & Avery, 2002), is an open problem in evolutionary biology.

Consider a stress response network module, consisting of a stress-sensing transcriptional regulator and its stress-protective gene target, which has arisen in a cell's genome. Similar modules, such as *Tn10* (Hillen & Berens, 1994), toxin-antitoxin systems (Yamaguchi *et al*, 2011), or bypass signaling (Hsieh & Moasser, 2007), can arise rapidly by recombination, horizontal gene transfer, or inhibitor-mediated alternate pathway activation. Considering their impact on microbial and cancer drug resistance, it is important to know how reproducibly and how quickly such stress defense networks can adapt (Lobkovsky & Koonin, 2012). Yet, we currently lack quantitative, hypothesis-driven understanding of how initially suboptimal stress defense modules evolve inside the host genome, especially in the presence of gene expression noise (Balázsi *et al*, 2011; Munsky *et al*, 2012; Sanchez & Golding, 2013). Although

1 Department of Systems Biology - Unit 950, The University of Texas MD Anderson Cancer Center, Houston, TX, USA
2 Center for Computational Biology & Department of Molecular Biosciences, University of Kansas, Lawrence, KS, USA
3 Department of Physics & Astronomy, Rutgers University, Piscataway, NJ, USA
4 Department of Chemistry and Chemical Biology, Harvard University, Cambridge, MA, USA
5 School of Biomedicine, Far Eastern Federal University, Vladivostok, Russia
6 BioMaPS Institute for Quantitative Biology, Rutgers University, Piscataway, NJ, USA
7 Laufer Center for Physical & Quantitative Biology, Stony Brook University, Stony Brook, NY, USA
8 Department of Biomedical Engineering, Stony Brook University, Stony Brook, NY, USA
*Corresponding author. Tel: +1 631 632 5414; Fax: +1 631 632 5405; E-mail: gabor.balazsi@stonybrook.edu
†These authors contributed equally to this study

network evolution theory (Kauffman, 1993; Mason *et al*, 2004; Kashtan & Alon, 2005) and laboratory evolution experiments (Lenski & Travisano, 1994; Beaumont *et al*, 2009; Tenaillon *et al*, 2012; Toprak *et al*, 2012; Lang *et al*, 2013) have generated important insights, they have provided largely descriptive, *a posteriori* interpretations. Now there is a growing need for predictive, hypothesis-driven, quantitative understanding of gene network evolution, which requires making *a priori* predictions of mutation effects and evolutionary dynamics that are tested experimentally (Wang *et al*, 2013). One option could be to study the evolution of small natural regulatory modules (Dekel & Alon, 2005; Hsu *et al*, 2012; Quan *et al*, 2012; van Ditmarsch *et al*, 2013). However, connections of natural regulatory modules with the rest of the genome can be significant (Maynard *et al*, 2010) and poorly characterized, thus making predictive, quantitative understanding difficult. Synthetic gene circuits (Elowitz & Leibler, 2000; Gardner *et al*, 2000; Stricker *et al*, 2008; Moon *et al*, 2012; Nevozhay *et al*, 2013) represent a better alternative, since they are small, consist of well-characterized components, and typically lack direct regulatory interactions with the host genome. However, it is unclear whether the evolution of synthetic gene circuits (Yokobayashi *et al*, 2002; Sleight *et al*, 2010; Poelwijk *et al*, 2011; Wu *et al*, 2014) can be predicted *a priori*, especially with regard to gene expression heterogeneity.

We recently characterized the dynamics and fitness effects of gene expression for a synthetic two-gene "positive feedback" (PF) circuit (Fig 1A) integrated into the genome of the haploid single-celled eukaryote *Saccharomyces cerevisiae* (Nevozhay *et al*, 2012). This synthetic gene circuit consists of a well-characterized transcriptional regulator (*rtTA*) and an antibiotic resistance gene (*yEGFP::zeoR*). In the presence of tetracycline-analog inducers such as doxycycline, rtTA activates both itself and *yEGFP::zeoR* by binding to two *tetO2* operator sites in two identical promoters (Fig 1A). This positive feedback is noisy, however, and thus, only a fraction of cells switch to high expression of rtTA and yEGFP::zeoR. These cells benefit from high gene expression, which protects them from the antibiotic zeocin. Meanwhile, the same cells experience a cost from rtTA activator expression toxicity, causing a tradeoff when zeocin is present (Nevozhay *et al*, 2012). The fitness (division rate) of any individual cell is the product of its rtTA expression cost and yEGFP::zeoR expression benefit (Nevozhay *et al*, 2012), which varies from cell to cell. Thus, quantitative knowledge of dynamics and fitness effects makes the PF gene circuit an excellent model for studying gene network evolution in tradeoff situations. Its design separates stress (zeocin) from its adjustable cellular response (inducible *yEGFP::zeoR* expression), facilitating predictive, quantitative understanding of how a stress response module adapts inside the host genome.

Here, we used our quantitative knowledge of the PF gene circuit to predict *a priori* the timing and mechanisms of its initial adaptation to several constant environments (squares in Fig 1B) corresponding to various stress-response imbalance scenarios. We tested these predictions with experimental evolution, followed by sequencing to identify the mutations that establish in the population, depending on the imbalance between the environmental stress and the intracellular response. In this way, we tested how different mutations can readjust the response of a network module with inherent tradeoff, to match the stress and minimize the cost in each specific environment. These results could help us understand how fast and through what mechanisms drug resistance emerges or deteriorates in the process of network evolution, and could help the future design of synthetic gene circuits that resist evolutionary degradation.

Results

The PF gene circuit can mimic various scenarios of stress-response imbalance

We considered the following disparities between the external stress and the activity of a stress defense module: (i) the module responds gratuitously to a harmless environmental change; (ii) the module cannot respond to harmful stress when needed; and (iii) the module responds to stress, but suboptimally. To mimic these scenarios using the PF gene circuit in yeast, we relied on the separability of stress and response, adjusting two environmental factors with known fitness effects (Nevozhay *et al*, 2012): inducer doxycycline and antibiotic zeocin (Fig 1). Hereafter, DxZy will denote environmental conditions, with x and y indicating doxycycline and zeocin concentrations, respectively. The antibacterial compound doxycycline has negligible effect on yeast (Wishart *et al*, 2005), but causes squelching toxicity in engineered PF cells when bound to rtTA (Gari *et al*, 1997; Nevozhay *et al*, 2012). Zeocin is a broad-spectrum DNA-damaging antibiotic (Burger, 1998) that acts on bacteria and eukaryotes.

First, the presence of inducer doxycycline alone corresponds to scenario (i): costly, futile response of some (Fig 1B, DiZ0) or most (Fig 1B, D2Z0) cells that start expressing the PF genes. The cost of response slows the cell division rate of responding, high expressor cells compared to non-responding, low expressor cells (Nevozhay *et al*, 2012). Consequently, the division rate of individual yeast cells can differ drastically from the overall population growth rate. To capture these differences between single cell- and population growth rates, we constructed a population fitness landscape (three-dimensional gray surface in Fig 1B) and cellular fitness landscapes (colored panels in Fig 1B). The population fitness landscape maps the overall population growth against the two environmental variables, doxycycline and zeocin concentrations. Cellular fitness landscapes depict the division rate of single cells versus their gene expression level in a given combination of doxycycline and zeocin. As described in the Appendix, we inferred these landscapes directly from growth rate and gene expression measurements (Appendix Fig S1A) in 13 different combinations of doxycycline and zeocin.

Second, the presence of antibiotic zeocin alone (Fig 1B, D0Z2) corresponds to the lack of response when needed, as in scenario (ii). Finally, the presence of both inducer and antibiotic (Fig 1B, DiZ2 and D2Z2) corresponds to scenario (iii) where the fraction of responding, slower-growing cells ensures cell population survival during antibiotic treatment, but the response is in general suboptimal.

Altogether, the PF gene circuit is a well-characterized module lacking direct regulatory interactions with the yeast genome. It exemplifies typical tradeoffs between the benefits and costs of gene expression in stress response networks. Importantly, the benefits and costs are independently tunable for the PF gene circuit, making it possible to predict and test their evolution toward optimality.

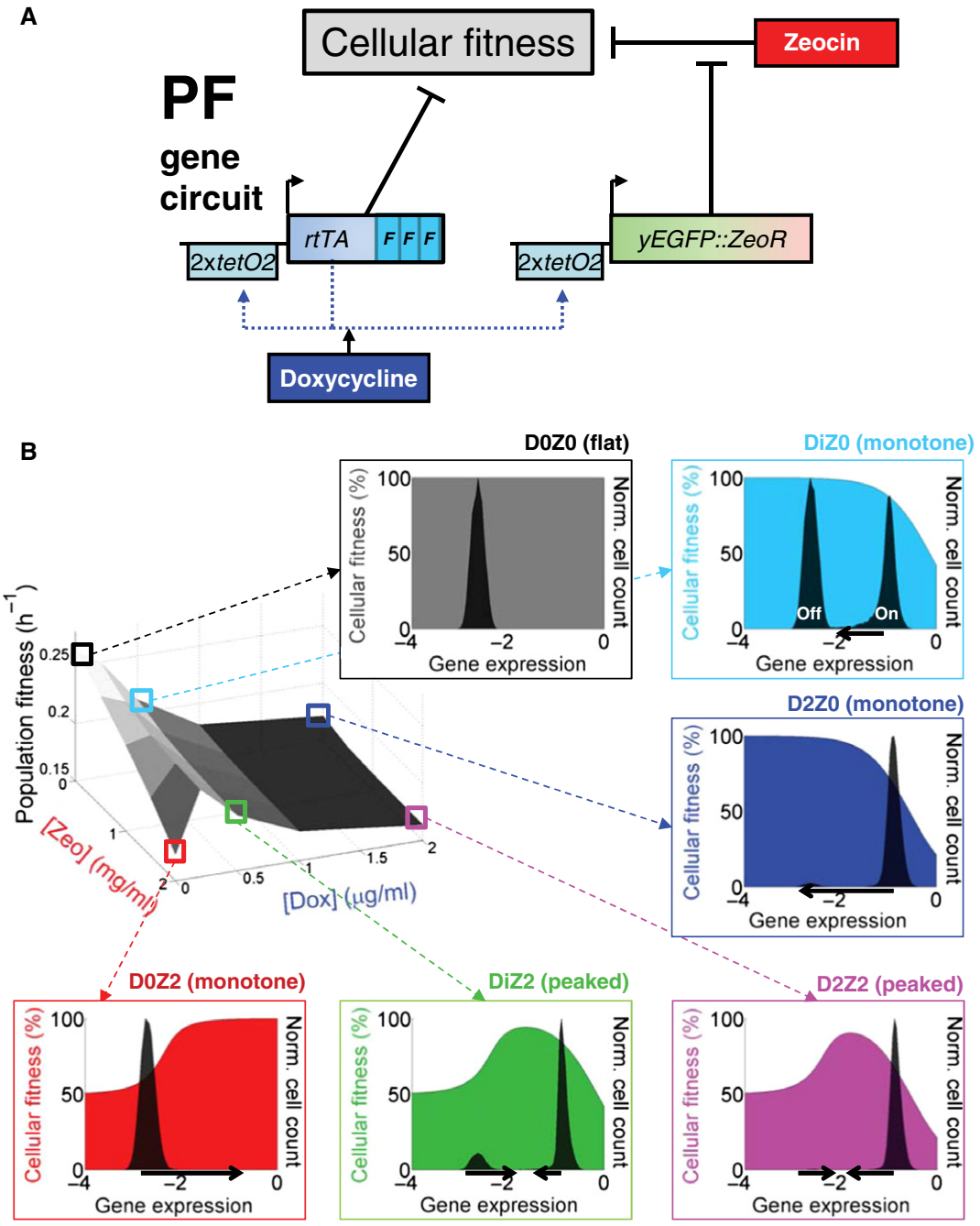

Figure 1. The PF synthetic gene circuit: fitness and gene expression characteristics.

A The PF synthetic gene circuit (Nevozhay *et al*, 2012) consists of two components. First, the *regulator* reverse tet-trans-activator (rtTA) (Urlinger *et al*, 2000) is a reverse-*tetR* gene fused to three F activator domains (cyan rectangles), which are shorter versions of the VP16 activator (Baron *et al*, 1997). The *target gene yEGFP::ZeoR* consists of the fluorescent reporter *yEGFP* fused to the drug resistance gene *zeoR* (Gatignol *et al*, 1988) that binds and inactivates zeocin, a bleomycin-family antibiotic. Unbound zeocin generates DNA double-strand breaks, causing cell cycle arrest and potentially cell death. Doxycycline added to the growth medium diffuses freely through the cell wall and binds to rtTA dimers. Inducer-bound rtTA undergoes a conformational change that results in strong association with two *tetO2* operator sites upstream of each of the two *tetreg* promoters (Becskei *et al*, 2001), activating both regulator and target gene expression, while causing toxicity by squelching.

B Costs and benefits of PF gene circuit components were determined by measuring cell population growth rate (population fitness) versus two environmental factors: inducer doxycycline and antibiotic zeocin. Each point on the population fitness landscape (three-dimensional gray surface on the left) is an average of cellular fitness values (color-shaded slopes in the surrounding plots) as cells stochastically move within gene expression distributions (black histograms in the surrounding plots). Gene expression is measured as $\log_{10}$(fluorescence) (arbitrary units). DxZy denotes the environment (the x and y following D and Z indicate µg/ml doxycycline and mg/ml zeocin concentrations, respectively, with Di = 0.2 µg/ml doxycycline). Cellular fitness (cell division rate) is a function of gene expression for each cell in each environment DxZy. It is inferred from the population fitness, based on a biochemical model (Nevozhay *et al*, 2012); see the Appendix. The black arrows beneath cellular fitness landscapes illustrate selection pressures pushing the gene expression distribution toward higher fitness.

Predicting the first evolutionary steps in constant environments

We asked whether the PF cellular and population fitness landscapes (colored squares and panels in Fig 1B; Appendix Fig S1A; Appendix Table S1) could predict evolutionary trends in specific environments. For example, in the D2Z0 environment, most cells are far from their fitness maximum, which is at low expression. If a mutation could push cells downward in expression, toward their fitness maximum (horizontal arrow in Fig 1B, D2Z0 panel), then they should grow faster. Mutations that either *abolish* or *weaken* rtTA toxicity could achieve this effect. Let us call these mutation types "knockout" (K) and "tweaking" (T) mutations, respectively (Fig 2A; Appendix Fig S1B). On the other hand, in the D0Z2 environment cells should benefit from mutations that diminish the effect of the antibiotic. This could happen in various ways, for example by upregulation of native stress-response mechanisms; or by increasing yEGFP::zeoR expression. Let us call these latter mutation types "generic" (G) drug resistance mutations (Fig 2A; Appendix Fig S1B). In all these cases, mutant cells can improve their fitness by unidirectionally lowering or increasing PF gene expression. However, in certain conditions (such as DiZ2), when the cells form two subpopulations that flank the cellular fitness peak, a single-directional expression change is not optimal. This is because a one-way expression shift can only move one subpopulation toward the fitness peak, while the other subpopulation must necessarily move away from it. Instead, optimally the two subpopulations should approach each other, both moving toward the fitness peak (horizontal arrows in Fig 1B, DiZ2, D2Z2 panels).

How would the PF cells evolve to adapt in specific combinations of doxycycline and zeocin? Mutations of any type (K, T, G) can arise spontaneously, then establish in the population, and compete with each other depending on two requirements. First, the mutation type must be available (genetic changes causing the phenotype must exist). Second, since we consider large populations, the mutation should be beneficial, improving fitness in the given environment. Despite these intuitive expectations, it is unclear how many mutations of each type will establish in each condition, and how fast.

To address these questions *in silico*, we developed two complementary modeling approaches: a simple mathematical model and a detailed computational simulation framework (see the Computational Models.zip file and the Appendix for detailed descriptions). The two models serve to test the robustness of results to various modeling approaches. The simple model was more general and faster, allowing more extensive parameter scans. On the other hand, the simulation framework allowed testing how specific details of experimental evolution would affect the evolutionary dynamics, and provided more detailed results. We initiated both models with a population of ancestral (wild-type) PF cells, aiming to find out the number and type of mutations that establish and when the ancestral genotype disappears. We modeled 20 days of evolution in each environment indicated by the colored squares in Fig 1B.

The simpler model described population dynamics by a system of ordinary differential equations (ODEs), assuming constant population size and mutation rate. We characterized wild-type and mutant cells by a single parameter: their fitness (exponential growth rate), determined from the fitness landscapes in Fig 1B. For example, we assumed that K mutants had cellular fitness corresponding to null expression in Fig 1B. T-type mutant cells altered their fitness randomly to a level corresponding to intermediate expression on the cellular fitness landscapes. Finally, G-type mutants increased their fitness randomly, up to a level they would have without zeocin. This simpler model could predict how fast the wild-type genotype disappears from the population. It could also forecast the mutation type (K, T, G) that predominantly replaces the wild type in each condition. However, it could not predict the number of distinct mutant alleles in the evolving population. Moreover, it lacked potentially important experimental details, such as periodic resuspensions and phenotypic switching.

To test the importance of such additional details, the detailed simulation framework captured multiple experimentally relevant aspects of evolution. For example, cells could switch between On and Off states with experimentally inferred rates (Appendix Table S1). K, T, and G mutations with altered switching and growth rates entered the population as single cells at a constant, but adjustable rate μ per cell per generation (Fig 2A; Appendix Fig S1C). K-type mutants could not switch On, and thus had no cellular fitness costs in doxycycline. T-type mutants switched On at a randomly reduced rate, and thus had diminished cellular fitness costs from PF gene expression. G-type mutant cells had randomly increased drug resistance without any change in switching rates. We simulated periodic resuspensions by repeatedly reducing the cell population size to 10^6. We considered cells to be initially drug- and inducer-free, and allowed them to gradually take up zeocin and doxycycline. This simulation framework could predict the number of distinct mutant alleles, in addition to the characteristics predicted by the simpler model.

Both models had three free parameters: the rate of potentially beneficial mutations μ, and the input probabilities P(G) and P(T) of a given mutation being of type G or T, respectively. Once known, these parameters also define the probability of a mutation to be of type K: $P(K) = 1 - P(G) - P(T)$. We note the difference between the rate and probability of a mutation: for example, the probability of P(K) could be equal to 1, while its rate $\mu P(K)$ is much < 1 per genome per generation. Figure 2A depicts the effect of each mutation type, illustrating the relationships among the free parameters. We extracted the rest of the parameters (Appendix Table S1) from experimental measurements (see the Appendix) and kept them fixed.

Using these models, we studied how the three free parameters affected three features of evolutionary dynamics: the ancestral genotype's half-life, as well as the type and number of mutant alleles in each condition (Fig 2; Appendix Figs S2 and S3). We started by studying the ancestral genotype's half-life in each model, scanning each free parameter systematically (Fig 2B; Appendix Figs S2B and S3B). The models consistently indicated (Fig 2B) that the ancestral genotype disappeared fastest in conditions with steep monotone cellular fitness landscapes (Fig 1B, D0Z2 and D2Z0). In contrast, the ancestral genotype remained in the population longer in peaked cellular fitness landscapes (Fig 1B, D2Z2 and DiZ2). Finally, the majority of cells were still genetically ancestral after 20 days in DiZ0, which has the most gradual cellular fitness landscape (Fig 1B, DiZ0). The time when the ancestral genotype disappeared in various environments depended differently on the mutation probabilities P(K), P(T), P(G) (Appendix Fig S3B). For example, the ancestral genotype disappeared later in D2Z2 when we lowered P(T). Likewise, lowering P(G) prolonged the ancestral genotype's

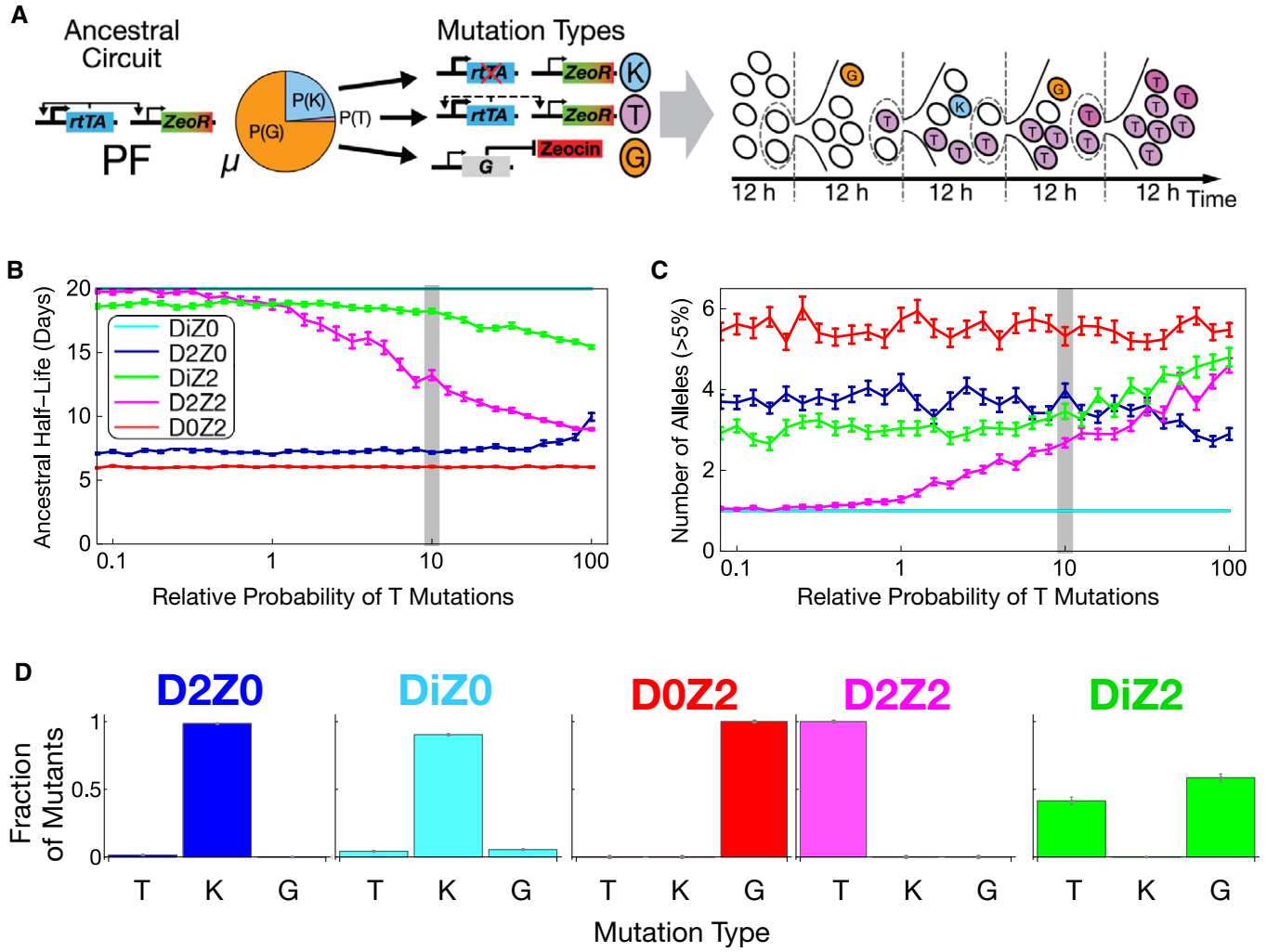

Figure 2. Simulation framework predicts evolutionary dynamics.

A Simulating the initial steps of evolution. Three types of potentially beneficial mutations (with an overall rate μ) enter the ancestral population of yeast cells that initially carry the intact PF gene circuit. Each cell can divide and mutate, producing new genotypes with altered fitness that can belong to three different types. The first two types are knockout (K) and tweaking (T) mutations. They eliminate rtTA's regulator activity and toxicity completely or partially, respectively. The third type includes extra-rtTA or generic (G) mutations that cause zeocin resistance independently of rtTA. In the models, we consider exponential growth with random elimination of cells or periodic resuspensions to control population size. Empty circles represent intact PF cells, while blue, magenta, and orange circles represent K, T, and G mutants, respectively. These mutations can arise, be lost, or expand in the population.

B The speed at which mutants take over the population in each simulated condition is measured as the ancestral genotype's half-life (the time until only 50% of the population carries the ancestral genome). N = 100; mean ± SEM in each simulated condition: D2Z0, DiZ0, D0Z2, D2Z2, and DiZ2. In these plots, we fixed $\mu_{-Z} = 10^{-6.2}$ or $\mu_{+Z} = 10^{-5.4}$/genome/generation (for no zeocin and zeocin, respectively) and P(G) = 0.75. Therefore, P(T) = 0.25 − P(K). On the horizontal axis, we show the probability of T mutations among intra-rtTA mutations: P*(T) = P(T|¬G), which scales P(T) four-fold up such that its maximum is 1 instead of 0.25. The gray bar denotes the value used for time course simulations in subsequent figures. The parameter set for the gray bar on this and the following panels is P(T) = 0.025; P(K) = 0.225; and P(G) = 0.75.

C Number of established mutations with frequency > 5% at day 20. N = 100; mean ± SEM in each simulated condition: D2Z0, DiZ0, D0Z2, D2Z2, and DiZ2. Parameters, axes, and gray bar: as in (B).

D Population fractions of T-, K-, and G-type mutations at day 20, for the parameters corresponding to the gray bar, as indicated above.

presence in the populations in D0Z2. These observations confirmed the expectation that the most beneficial mutation in each condition dictates evolutionary dynamics. Overall, we hypothesized based on these results that the ancestral PF gene circuit should disappear fastest in D2Z0 and D0Z2, followed by DiZ2 and D2Z2, and finally in DiZ0. Making these predictions required quantitatively understanding the fitness properties and genetic structure of the PF gene circuit. Without modeling, it would have been impossible to obtain quantitative estimates of the speeds at which mutants establish and take over the evolving population.

In general, K, T, and G allele frequencies at the end of simulated time courses did not match the input probabilities of P(K), P(T), and P(G) mutations. Rather, each condition favored different mutation types as long as they were available (Fig 2D; Appendix Figs S2 and S3). For example, in D2Z0, nearly all mutations were K-type even if K mutations were unlikely to enter the population. T

mutations established exclusively in D2Z2, while in DiZ2 they appeared alongside G mutations. In DiZ0, K or T mutations established late and spread slowly, with parameter-dependent relative fractions. Finally, only G alleles could establish in D0Z2. To conclude, both models predicted the environment-specific dominance of various mutation types at 20 days, irrespective of the relative supplies of different mutation types. The most likely cause is each condition selecting one mutation type so strongly that the final outcome of evolution (but not its dynamics) becomes quasi-deterministic. The long-term dominance of specific mutants in each condition might have been intuitively inferable from the fitness properties and genetic structure of the PF gene circuit. However, modeling is indispensable to understand the evolutionary dynamics of mutants arising, establishing and competing before reaching the final state.

Finally, we used the simulation framework to determine the number of alleles over 20 days in each condition (Fig 2C). This is perhaps the least intuitive result that could not have been predicted without computation. The simulations indicated that the number of alleles exceeding a certain frequency depended strongly (sometimes non-monotonically) on the overall mutation rate as well as the availability of individual mutations (Appendix Fig S3A). The dependence of allele numbers on simulation parameters should allow parameter estimation once experimental allele data are available.

In summary, based on mathematical and computational models, we hypothesized that the ancestral PF gene circuit should disappear from the population fastest in conditions D2Z0 and D0Z2, followed by D2Z2 and DiZ2, and lastly DiZ0. In addition, we conjectured that K, T, and G mutations should predominate in D2Z0, D2Z2, and D0Z2, respectively, whereas mixtures of T and G genotypes should prevail in DiZ2. Mutations (K or sometimes T) should be slow to establish in DiZ0, causing the ancestral genotype to remain in the majority even at 20 days. To test these hypotheses, we evolved three replicate PF yeast cell populations in five conditions (DiZ0, D2Z0, D0Z2, DiZ2, D2Z2) corresponding to the colored squares on the population fitness landscape in Fig 1B. We also evolved cells in the control condition D0Z0, where we found only one barely detectable, low-frequency synonymous substitution (Appendix Table S2). We observed directly the relationship between gene expression and fitness by daily fluorescence and cell count measurements over the course of these experiments. For various experiments and on multiple days, we collected samples for whole-genome and traditional (Sanger) sequencing to reveal the mutations underlying the observed gene expression changes.

Scenario (i): reproducible circuit failure from gratuitous circuit response

To test the fate of a new stress defense module that becomes costly by gratuitously responding to an otherwise harmless environmental change, we grew PF yeast cells in inducer doxycycline without antibiotic (D2Z0), resuspending every 12 h. In this condition, fluorescence first rose and then began to decline toward the basal level in < 1 week (~40 generations) for all three replicate populations (Fig 3A). The fluorescence decline continued until gene expression was indistinguishable from that of uninduced cells by the end of the experiment, consistent with the effect of K-type mutations. As fluorescence levels dropped, population growth rate increased significantly (see the Source Data for Fig 3A), indicating that the initial cost of futile response disappeared. These concurrent fluorescence and fitness changes agreed with the leftward hill climb on the blue landscape in Fig 1B (black arrow underneath D2Z0) expected for K-type mutations.

To uncover the genetic mechanism(s) underlying these fluorescence and fitness changes, we combined whole-genome and Sanger sequencing (see the Appendix). Our analysis revealed four competing mutations inside the rtTA coding sequence that jointly accounted for most of replicate population #1 already at Day 9 (Fig 3C and D "12 h-1"; Appendix Table S3), and eliminated the ancestral genotype by the end of the experiment. The same happened in the other two replicate experiments as well (Fig 3C–E "12 h-2,3"; Appendix Table S3). This is consistent with computationally predicted K-type mutations eliminating rtTA toxicity, along with its transcription-activating function. We detected no mutations in other parts of the genome, although we cannot rule out the possibility of mutations in repeat regions or large duplications/deletions that are notoriously difficult to detect by whole-genome sequencing (Appendix Fig S4D and E). We repeated the evolution experiment with 24-h resuspensions and observed similar fluorescence and fitness changes, along with rtTA coding sequence mutations, except that they occurred faster (Fig 3C "24 h-1,2,3"; Appendix Fig S4A–C, Appendix Table S3). Four of these mutations (three STOP codons

Figure 3. Evolutionary dynamics of PF cells in D2Z0 and DiZ0, corresponding to scenario (i): futile response to harmless signal.

A Time-dependent changes in the fluorescence distributions (blue heatmaps), average fluorescence (blue circles), and average, mixed population fitness (blue squares). Data were collected as PF cells evolved in condition D2Z0 (2 μg/ml doxycycline and no zeocin) in three replicate experiments. Average fluorescence and fitness values in control condition D0Z0 are also shown as black crosses for reference. Both the fluorescence (P = 0.00019) and fitness (P = 0.003959) were significantly different in populations evolving in D2Z0 compared at Days 4 and 21 (t-test, see the Materials and Methods).

B The same measurements as in (A), but for PF cells evolving in condition DiZ0 (0.2 μg/ml doxycycline and no zeocin, cyan heatmaps) in three replicate experiments. The fluorescence (P = 0.0144526) was significantly different, but the fitness (P = 0.2459) was not in populations evolving in DiZ0 when compared at days 4 and 21. Pairwise comparisons with the same days in D0Z0 showed no significant fitness differences (see the source data).

C Intra-rtTA mutations observed in conditions D2Z0 (blue lines) and DiZ0 (light blue lines) mapped along the rtTA activator within the PF gene circuit sequence. The five lines of annotation indicate the following: (i) basepair coordinates relative to the rtTA translation start site (+1); (ii) nucleotide substitution; (iii) amino acid substitution; (iv) in which experiment the allele was found; and (v) allele fractions at Day 19 inferred from sequencing. If there was a deletion or duplication, the first two lines represent its range. *: STOP codon; Δ: deletion; Dupl: duplication. No extra-rtTA mutations were identified in these conditions. Clones selected for phenotyping are underlined and numbered in blue.

D, E Time-dependent allele frequencies for mutations observed in conditions D2Z0 (D), and DiZ0 (E), replicate experiment #1. The way we used sequencing data to draw allele frequencies and the lines connecting them is explained in the Mutation time course reconstruction section of the Materials and Methods.

F, G Time-dependent allele frequencies from simulations using mutation parameter values reflecting experimental conditions.

Source data are available online for this figure.

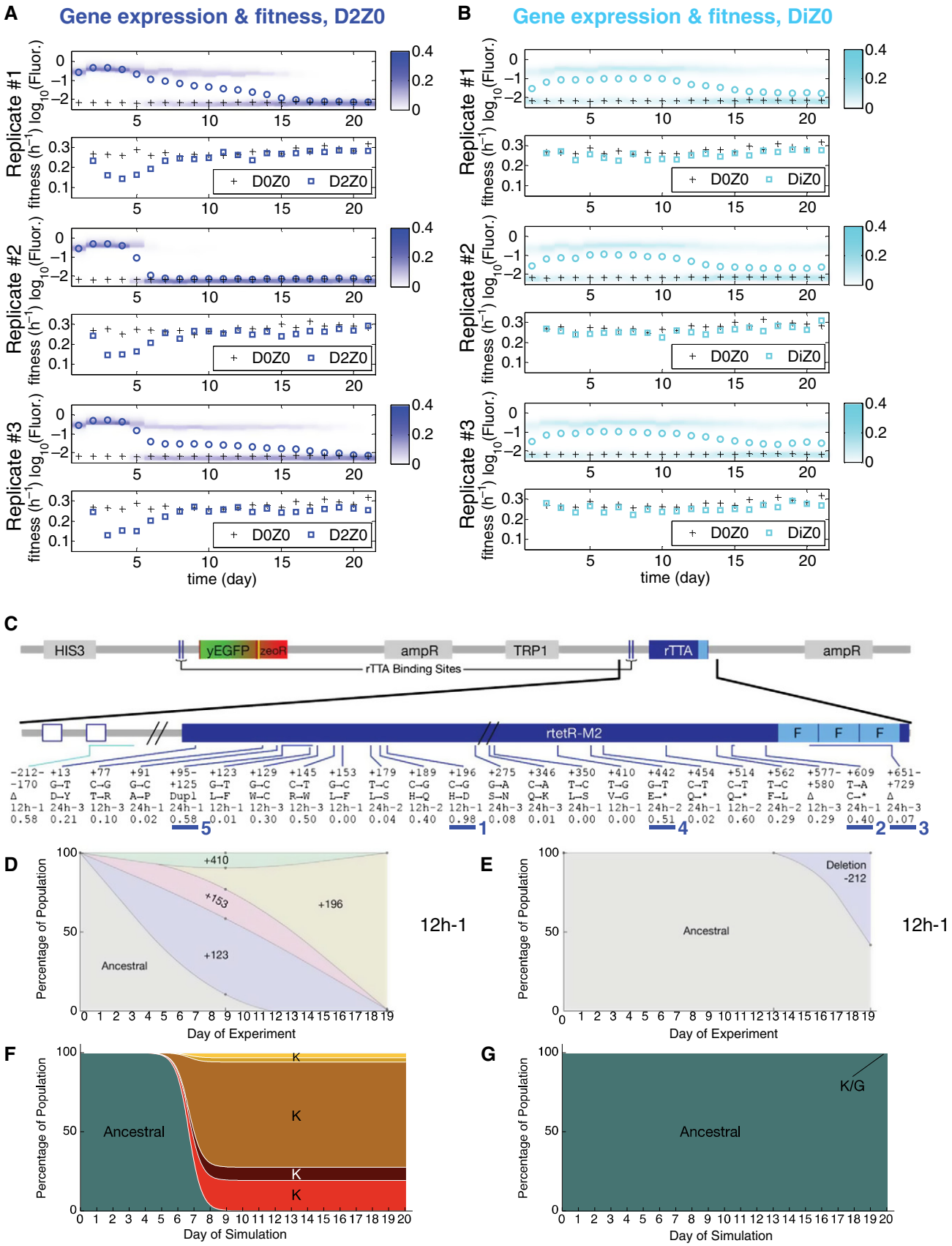
A
Gene expression & fitness, D2Z0
B
Gene expression & fitness, DiZ0
Replicate #1
Replicate #2
Replicate #3
fitness (h−1) log10(Fluor.)
D0Z0
D2Z0
DiZ0
time (day)
C
HIS3
yEGFP
zeoR
ampR
TRP1
rTTA
rTTA Binding Sites
rtetR-M2
D
E
Percentage of Population
Day of Experiment
Ancestral
+410
+153
+196
+123
Deletion -212
12h-1
F
G
Day of Simulation
K
K/G

Figure 3.

and a 78-base pair deletion) truncated and eliminated all three activator domains of rtTA, further supporting the K-type loss of rtTA function.

Decreasing the inducer (doxycycline) concentration from 2 to 0.2 μg/ml should diminish rtTA toxicity. Selection in this condition should be weaker (Fig 1B), lowering the chances of beneficial mutations establishing in DiZ0 compared to D2Z0. To test these predictions, we evolved three cultures in the DiZ0 condition (Fig 3B). In agreement with computational predictions (Fig 2A and B; Appendix Figs S2 and S3), the fraction of On cells started declining slowly only toward the end of the experiment. This resulted in a statistically significant change in fluorescence, but not in fitness. Moreover, Sanger sequencing at the end of the experiment revealed a single intra-circuit deletion at 58% frequency (Fig 3C), which eliminated one of the two *tetO2* operator sites upstream of rtTA. This suggests a T-type mutation (since one *tetO2* site remained intact) targeting a regulatory region rather than protein-coding sequence. We detected no mutations elsewhere in the genome.

In summary, these experimental observations confirmed the computational predictions that a steep, monotonically decreasing cellular fitness landscape (Fig 1B, D2Z0, blue shading; Fig 3F and G) reproducibly selects for lower gene expression. The effect of these mutations is to decrease gene expression unidirectionally by either eliminating or reducing the fraction of On cells. Thus, deleterious network activation favors mutations that prevent or reduce switching into the slow-growing On state. We selected five individual genotypes (underlined with blue in Fig 3C) for testing whether their gene expression and fitness are consistent with K-type mutations (see below the section on phenotyping).

Scenario (ii): gaining gene expression for an initially unresponsive gene circuit

To test what happens if a stress defense module cannot induce when needed during harmful stress, we grew cell populations in 2 mg/ml zeocin (D0Z2). The lack of inducer in this condition forced all cells to be in the drug-sensitive Off state. Consequently, the tradeoff between elevated expression and drug resistance specific to the PF gene circuit was absent in D0Z2. Early in the course of evolution, we observed a substantial, statistically significant drop in population fitness compared to untreated cells (Fig 4A), indicating the gene circuit's inability to respond to stress. Yet, some cells must have had enough drug resistance to survive, because the growth rates of cultures started to recover after $\sim$4 days (Fig 4A). At the same time, yEGFP::ZeoR expression increased significantly compared to control cultures maintained in D0Z0 (Fig 4A). This difference remained statistically significant even after correction for multiple comparisons, particularly toward the end of the experiment. We observed similar trends with 24-h resuspensions (Appendix Fig S5). Thus, the evolving cell population moved repeatedly upward in gene expression and drug resistance space, toward the cellular fitness maximum in Fig 1B (black arrow underneath D0Z2). In contrast, cells lacking the *zeoR* gene never recovered in the same level of zeocin, while cells with higher basal yEGFP::zeoR expression recovered faster (Appendix Fig S5C–E).

Next, we sought mutations explaining the observed fluorescence and fitness changes. In sharp contrast with D2Z0, we found no mutations in either rtTA or its regulatory region. Instead, we detected two extra-rtTA, but intra-circuit mutations overall in six replicate experiments (Fig 4D; Appendix Table S4), one of which eliminated a *tetO2* operator site upstream from *yEGFP::zeoR*, while the other was a synonymous substitution in an arginine codon within the *zeoR* coding region. Additionally, sequencing revealed multiple extra-circuit mutations (Fig 4B) and linkage between the intra-circuit *tetO2* deletion and some extra-circuit alleles (Fig 4B and D). This raised the possibility that intra- and extra-circuit mutations jointly detoxify the cells in a manner consistent with G-type mutations. The real number of extra-circuit mutations could be higher, considering the difficulty of detecting certain mutation types by high-throughput sequencing. In addition, some adaptation in D0Z2 could also have occurred through native stress responses or non-genetic selection of the high-expressing tail of the basal yEGFP::ZeoR distribution.

Altogether, these data suggest that as long as cells with a potentially beneficial, but inoperative module have some basal resistance to survive, they can later activate the module and acquire drug resistance by genetic mutations (Charlebois *et al*, 2011). Apparently, this happens through mutations both inside and outside of the module, genetically integrating it with the host. This effect seems dependent on the presence of *zeoR*, since cells lacking this gene do not survive in D0Z2 (Appendix Fig S5C and D). An interesting question is whether drug resistance gained from these mutations involves some cost. To answer this question and test whether the mutants are indeed G-type, we selected and characterized six individual genotypes underlined with red in Fig 4D (see the section on phenotyping below).

Scenario (iii): optimization of gene expression under opposing evolutionary pressures

To test what happens when a module responds to stress non-optimally, we exposed the cells to both inducer and antibiotic. In these conditions, there is a cellular fitness peak at intermediate gene expression (Fig 1B, DiZ2 and D2Z2, green and magenta shading), in contrast to the monotone cellular fitness landscapes in conditions with only inducer (D2Z0 and DiZ0) or only antibiotic (D0Z2). The cellular fitness peak indicates opposing selection pressures from zeocin toxicity and the fitness cost of rtTA expression: zeocin selects for increased gene expression, while rtTA toxicity selects for diminished rtTA function and thus decreased gene expression (Fig 1B, arrows underneath DiZ2 and D2Z2). These selection pressures act on two cell subpopulations flanking a cellular fitness peak (Fig 1B, D2Z2). Therefore, fitness improvement in DiZ2 and D2Z2 requires adaptation toward an intermediate "sweet spot" of expression. K mutations cannot achieve this since they completely disrupt rtTA function.

In D2Z2, average fluorescence decreased while fitness increased significantly for all replicate cultures (Fig 5A), albeit by a lesser extent and more slowly than in D2Z0 (Fig 3A), as predicted computationally. Sequencing has uncovered only two competing alleles from one replicate culture, each affecting a distinct PF gene circuit component. Sequencing samples from the other two replicate experiments then revealed D2Z2-specific mutations that repeatedly occurred in the same rtTA loci: the 5′ untranslated rtTA region and the 225th basepair of rtTA (Fig 5C; Appendix Fig S6A and B;

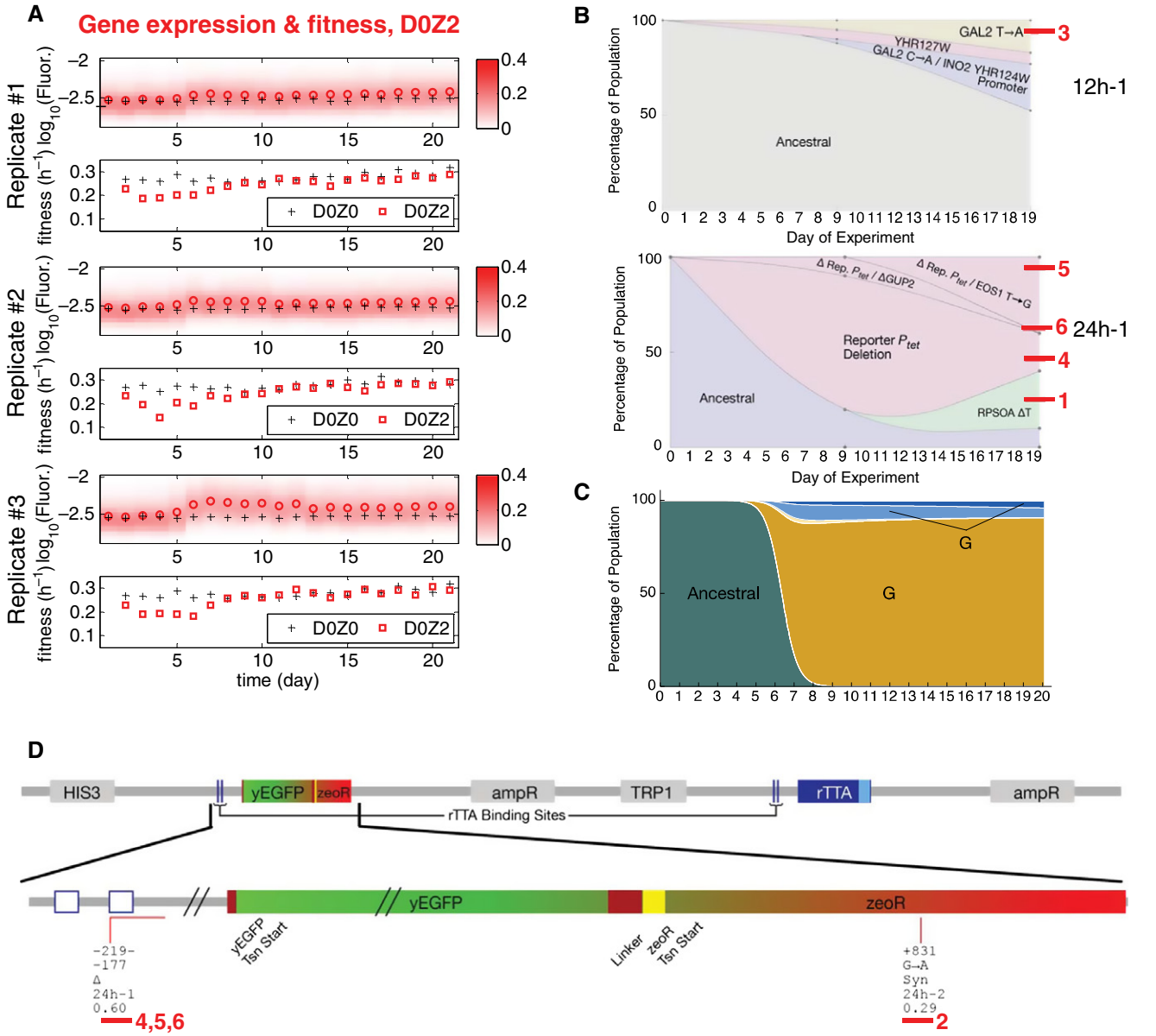

Figure 4. Evolutionary dynamics of PF cells in D0Z2, corresponding to scenario (ii): lack of response when needed.

A Time-dependent changes in the fluorescence distributions (red heatmaps), average fluorescence (red circles), and average, mixed population fitness (red squares) as PF cells evolve in condition D0Z2 (no doxycycline and 2 mg/ml zeocin) in three replicate experiments. Black crosses, as in Fig 3. Both the fluorescence (P = 0.014323) and fitness (P = 0.002244) were significantly different in populations evolving in D0Z2 when compared at days 4 and 21 (dependent samples t-test, see the Materials and Methods). In addition, at many time points, the fluorescence difference from the ancestral PF was statistically significant (independent samples t-test, see the Materials and Methods). These statistical differences persisted even after correcting for multiple comparisons. The same was true for fitness at early time points (up to Day 6).

B Time-dependent allele frequencies for mutations observed in condition D0Z2, replicate #1. Top: whole-genome sequencing from a 12-h resuspension experiment. Bottom: whole-genome sequencing combined with Sanger sequencing of clonal isolates from the same 24 h resuspension experiment, indicating linkage between intra- and extra-PF mutations. Among the observed mutations, *INO2* is a regulator of phospholipid biosynthesis that lowers stress resistance, and *YHR127W* function is unknown, but is synthetic lethal with *ARP1*, which mediates resistance to multiple stresses. Red bars and numbers indicate clones selected for phenotyping. The way we used sequencing data to draw allele frequencies and the lines connecting is explained in the Mutation time course reconstruction section of the Materials and Methods.

C Time-dependent allele frequencies from simulations using mutation parameter values reflecting experimental observations.

D Extra-rtTA, but intra-circuit mutations observed in condition D0Z2 (red lines) mapped along *yEGFP::zeoR* within the PF gene circuit sequence. The five lines of annotation indicate the following: (i) basepair coordinates relative to the yEGFP::zeoR translation start site (+1); (ii) nucleotide substitution; (iii) amino acid substitution; (iv) which experiment the allele was found; and (v) allele fractions at Day 19 inferred from sequencing. If there was a deletion, the first two lines represent its range. Δ, deletion; Syn, synonymous. Two extra-rtTA, but intra-circuit mutations were identified in this condition. Clones selected for phenotyping are underlined and numbered in red.

Source data are available online for this figure.

Appendix Table S5). Another mutation truncated rtTA by a STOP codon in the last activator domain but left the two other domains intact, suggesting a T mutation with diminished rtTA function and toxicity, while still maintaining a zeocin-resistant, yEGFP::ZeoR-expressing subpopulation.

Next, we studied how lower but nonzero rtTA toxicity affects evolutionary dynamics for a peaked fitness landscape, propagating PF cells in 0.2 μg/ml doxycycline and 2 mg/ml zeocin (Fig 1B, DiZ2). The addition of zeocin selects against low-expressing Off cells, reshaping the bimodal distribution seen in DiZ0, so that the fraction of On cells increases in DiZ2 (compare black histograms overlaid with cyan and green shading, DiZ0 and DiZ2 in Fig 1B). These high expressors thus survive in stress and can maintain the population until more potent drug resistance mutations arise (Charlebois *et al*, 2011). Indeed, fitness decreased only slightly during evolution in DiZ2 (Fig 5B). After Day 7, fluorescence seemed to decrease slowly while fitness crept up throughout the time course. These changes were not statistically significant when we compared fitness and fluorescence values at Day 4 and Day 21 along the DiZ2 time course. However, we found that the fitness in DiZ2 was significantly lower than in D0Z0 at several time points, which remained true even after correcting for multiple comparisons.

DiZ2 was the only condition where mutations affecting both rtTA and extra-circuit loci established (Fig 5E). The intra-circuit mutation was a *tetO2* site deletion from the rtTA promoter, eliminating the other *tetO2* site compared to the deletion in DiZ0. Additionally, we detected three extra-rtTA mutations, one of them linked to the *tetO2* deletion. In general, these findings indicated that peaked fitness landscapes selected for T-type mutations, while also allowing for G-type mutations, as predicted computationally (Figs 2D and 5F and D). We confirmed these mutation types by testing whether the mutations weakened rtTA activity, without eliminating it (see below).

Phenotyping reveals fitness-improving network characteristics

In contrast to the D0Z0 control condition where fitness and gene expression changes were statistically non-significant (Appendix Fig S6D and E), these quantities changed significantly in other conditions tested (Figs 3, 4 and 5). These changes generally involved mixed populations composed of different genotypes competing with each other. To characterize individual genotypes in isolation, we measured gene expression levels and population fitness of clonal isolates from the last day of the evolution experiments.

First, we studied five clonal isolates from the last day of the D2Z0 time course (underlined in blue in Fig 3C), to test whether they carry K-type mutations. If this is true, then they should be uninducible and their fitness should not depend on doxycycline. Therefore, we quantitatively characterized the effect of doxycycline on the fluorescence and fitness of these clones. Thus, we defined the fitness effect of doxycycline as $\log_{10}$[(fitness with doxycycline)/(fitness without doxycycline)]. Likewise, we defined the effect of doxycycline on fluorescence as $\log_{10}$[(fluorescence with doxycycline)/(fluorescence without doxycycline)]. Based on these measures, we found that all five clones isolated from the D2Z0 inducer-only condition were fitter (Fig 6A, top panel) than the PF ancestor and were uninducible (Fig 6A, middle panel). These properties matched the characteristics of K-type mutations predicted computationally to dominate in D2Z0 (Fig 6A). Sanger sequencing of clonal isolates from the middle and the end of the D2Z0 evolution time course indicated that each K-type mutation occurred individually, without linkage to other mutations. Some of these clones were also fitter in D0Z0 compared to the ancestral strain, suggesting additional adaptation to growth in minimal medium (Lenski & Travisano, 1994; New *et al*, 2014) after eliminating the rtTA toxicity.

Next, we studied clonal isolates from the last day of the D0Z2 time course (Fig 4B and D) to test whether they are zeocin-resistant. We quantitatively characterized the effect of zeocin on the fitness of these clones as $\log_{10}$[(fitness with zeocin)/(fitness without zeocin)]. To determine whether zeocin resistance arose from higher yEGFP::zeoR expression, we also defined the gene expression increase in these clones as $\log_{10}$[(fluorescence of evolved clone in D0Z0)/(fluorescence of PF ancestor in D0Z0)]. We found that all clones isolated from the zeocin-only condition (underlined in red in Fig 4B and D) had higher fitness in zeocin (D0Z2) compared to ancestral PF cells (Fig 6B, top panel). The cause of zeocin resistance was higher *yEGFP::zeoR* gene expression even in the condition D0Z0, without zeocin (Fig 6B, middle panel and Fig 6E). These observations are consistent with G-type mutations, predicted computationally to dominate in D0Z2. *yEGFP::zeoR* gene expression in all clones shifted significantly upward, obeying the selection pressure (Fig 1B, black arrow underneath D0Z2). Some clones had two linked mutations, one of which was within the PF gene circuit, while the other was outside of it. We found no mutations for one zeocin-resistant clone

Figure 5. Evolutionary dynamics of PF cells in D2Z2 and DiZ2, corresponding to scenario (iii): suboptimal response.

A Time-dependent fluorescence distributions (magenta heatmaps), average fluorescence (magenta circles), and mixed population fitness (magenta squares) as PF cells evolve in condition D2Z2 in three replicate experiments. Black crosses, same as in Fig 3. Both the fluorescence (P = 0.0003157) and fitness (P = 0.010568) were significantly different in populations evolving in D2Z2 when compared at days 4 and 21. Statistical test: as above.

B The same measurements as in panel (A), but for PF cells evolving in condition DiZ2 in three replicate experiments. Neither fluorescence (P = 0.95), nor fitness (P = 0.087) was significantly different in populations evolving in DiZ2 when compared at days 4 and 21. Pairwise comparisons with the same days in D0Z0 showed significant fitness differences, many of which remained true even after correction for multiple comparisons.

C Intra-circuit mutations observed in conditions D2Z2 (magenta lines) and DiZ2 (green lines) mapped along the rtTA activator within the PF gene circuit sequence. The five lines of annotation indicate: (i) basepair coordinates relative to the rtTA translation start site (+1); (ii) nucleotide substitution; (iii) amino acid substitution; (iv) which experiment the allele was found; and (v) allele fractions at Day 19 inferred from sequencing. If there was a deletion, the first two lines represent its range. *, STOP codon; Δ, deletion. While no extra-rtTA mutations were identified in condition D2Z2, a few were found in DiZ2 (see E). Clones selected for phenotyping are underlined and numbered.

D, E Time-dependent allele frequencies for mutations observed in conditions D2Z2 (D) and DiZ2 (E), replicate #1. The way we used sequencing data to draw allele frequencies and the lines connecting is explained in the Mutation time course reconstruction section of the Materials and Methods.

F, G Time-dependent allele frequencies from simulations using mutation parameter values reflecting experimental conditions.

Source data are available online for this figure.

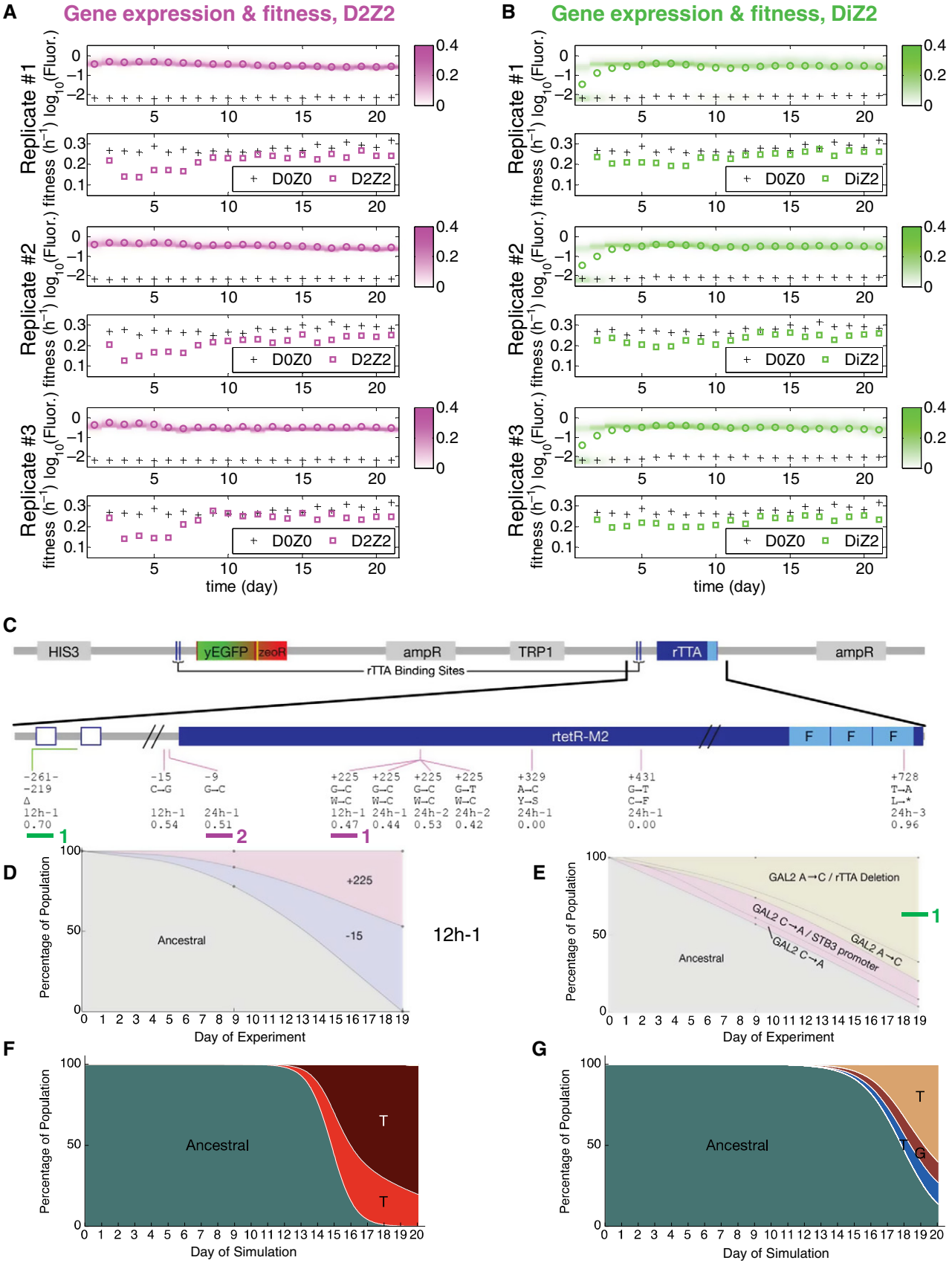
A
Gene expression & fitness, D2Z2
B
Gene expression & fitness, DiZ2
Replicate #1
Replicate #2
Replicate #3
log10(Fluor.)
fitness (h−1) log10(Fluor.)
D0Z0
D2Z2
DiZ2
time (day)
C
HIS3
yEGFP
zeoR
ampR
TRP1
rTTA
rTTA Binding Sites
rtetR-M2
F
-261-219 Δ 12h-1 0.70
-15 C→G 12h-1 0.54
-9 G→C 24h-1 0.51
+225 G→C W→C 12h-1 0.47
+225 G→C W→C 24h-1 0.44
+225 G→C W→C 24h-2 0.53
+225 G→T W→C 24h-2 0.42
+329 A→C Y→S 24h-1 0.00
+431 G→T C→F 24h-1 0.00
+728 T→A L→* 24h-3 0.96
D
Percentage of Population
Ancestral
+225
-15
12h-1
Day of Experiment
E
GAL2 A→C / rTTA Deletion
GAL2 C→A / STB3 promoter
GAL2 A→C
GAL2 C→A
F
T
G
Day of Simulation

Figure 5.

in any locus tested by Sanger sequencing, suggesting extra-circuit mutation(s) undetectable by either whole-genome or targeted Sanger sequencing. These results indicate that adaptation in D0Z2 recurrently involves mutations causing PF gene expression increase. This is surprising considering that mutations could have just upregulated native stress resistance pathways without involving the PF gene circuit.

Considering the original tradeoff between the cost of gene expression and benefit of drug resistance in the PF gene circuit, we asked whether a similar tradeoff may apply to drug-resistant genotypes evolved in D0Z2. Interestingly, adaptation by elevated basal yEGFP::zeoR expression tended to cause a fitness cost in D0Z0, when zeocin was absent (Fig 6B, bottom panel). The sources of these new fitness costs are unclear, but they are not rtTA-related because doxycycline was absent. This suggests that a novel tradeoff appeared between evolved stress resistance and growth in the absence of stress (Fig 6G). This new tradeoff is reminiscent of the original tradeoff in the ancestral PF gene circuit, where higher expression was also costly, but protective in the presence of antibiotic.

We similarly characterized the effects of doxycycline and zeocin on the fitness and gene expression of two clones isolated from D2Z2 experiments (underlined in magenta, Fig 5C). We found that both clones isolated from D2Z2 had reduced inducer sensitivities (Fig 6C), requiring higher doxycycline than the PF ancestor to reach a given gene expression level (Fig 6C, middle panel). Generally, the gene expression distributions of these clones were enriched in Off cells (Appendix Fig S7C and D). These changes were associated with lower doxycycline toxicity (Fig 6C, top panel, blue bars), while the cells still maintained drug resistance in doxycycline (Fig 6C, bottom panel, magenta bars). These characteristics were consistent with T-type mutations, as predicted computationally to dominate for peaked cellular fitness landscapes. Interestingly, in addition to the increase in Off cells, the On state moved to lower expression, toward the cellular fitness peak in the gene expression space (Appendix Fig S7C and D). We could still fully induce these clones by applying excessive (6 μg/ml) doxycycline levels with zeocin (Appendix Fig S7C and D). Interestingly, all cells were in the On state (fully induced) throughout the 20 days of evolution in D2Z2, but clones placed in D2Z2 were not. Taken together, these observations suggest that gene circuit bistability may have trapped mutant cells in the On state during evolution if the mutation arose in cells that were On.

Finally, we studied the single clone isolated from the DiZ2 experiments (*tetO2* deletion; underlined in green, Fig 5C). These cells required only slightly higher doxycycline levels for induction than the PF ancestor. Yet, once induced, they rose to higher mean expression level than the ancestor (Fig 6D; Appendix Fig S7A). Moreover, the two peaks in the bimodal gene expression histograms approached each other for this clone (Fig 6F; Appendix Fig S7A), both shifting toward the cellular fitness peak in Fig 1B, DiZ2 as dictated by selection. This is a unique example of noisy gene expression evolving under opposing selection pressures (Fig 1B, black arrows underneath DiZ2). Essentially, although evolution altered the gene expression, its distribution still remained bimodal, with a similar mean. While this mutation apparently alters rtTA function, it is different from the T-type mutations assumed in computational models (which did not account for shifting of peaks). This unique type of adaptation has no equivalent in phenotypically homogeneous populations with unimodal gene expression distributions.

To measure the phenotypic effects of the observed mutations in isolation from potential changes in the genetic background, we reconstructed the mutations $rtTA_{+225G\rightarrow C}$ (D2Z2 clone #1) and $rtTA_{-9G\rightarrow C}$ (D2Z2 clone #2) in the ancestral PF background (Appendix Fig S7C and D). The $rtTA_{+225G\rightarrow C}$ mutation was slightly inducible in the ancestral background, with a small high-expressing subpopulation at 2 μg/ml doxycycline. Moreover, we could reinduce this clone to nearly full expression using excessive doxycycline concentrations (6 μg/ml) in the presence of zeocin, suggesting that the reconstructed mutation $rtTA_{+225G\rightarrow C}$ lowered the dynamic range and sensitivity similar to the clonal isolate. Interestingly, however, the reconstructed $rtTA_{-9G\rightarrow C}$ mutation failed to induce even with excessive doxycyline concentrations, suggesting linkage and potential epistasis with some undetectable genetic extra-circuit mutation(s).

Overall, phenotyping validated the prevalence of K, T, G mutation types in different environments, as predicted computationally. Our observations also underscore the potential importance of noise-reshaping T-type mutations in artificial and natural evolution.

Figure 6. Gene expression and fitness characteristics of clonal isolates from various evolved populations.

A Phenotype of clones evolved in inducer doxycycline alone (D2Z0, "futile response"). The first bar ("Anc.") corresponds to the ancestral PF cells, and the other bars correspond to clonal isolates from the last time point of the D2Z0 experiment. Top panel: $\log_{10}$-ratio of fitness with doxycycline (D2Z0) relative to no doxycycline (D0Z0). Middle panel: $\log_{10}$-ratio of average fluorescence intensity with doxycycline (D2Z0) relative to no doxycycline (D0Z0). Bottom panel: $\log_{10}$-ratio of average population fitness of each evolved clone relative to the ancestor in no doxycycline (D0Z0). Error bars represent standard deviations around the mean. Stars denote significance at $P < 0.05$ (two-sided *t*-test).

B Phenotype of clones evolved in antibiotic zeocin alone (D0Z2, "lack of response when needed"). The first bar ("Anc.") corresponds to the ancestral PF cells, and the other bars correspond to mutants. Top panel: $\log_{10}$-ratio of fitness with zeocin (D0Z2) relative to no zeocin (D0Z0). Middle panel: $\log_{10}$-ratio of average fluorescence intensity of each evolved clone relative to the ancestor in no zeocin (D0Z0). Bottom panel: $\log_{10}$-ratio of average population fitness of each evolved clone relative to the ancestor in no zeocin (D0Z0). Error bars and stars as in (A).

C Phenotypes of two clones evolved in doxycycline and antibiotic zeocin (D2Z2, "suboptimal response"). The bars marked "A." correspond to the ancestral PF cells, and the other bars correspond to mutants. Top panel: $\log_{10}$-ratio of fitness with doxycycline (D2Zy) relative to no doxycycline (D0Zy) either with or without zeocin ($y = 0$ or $y = 2$). Middle panel: $\log_{10}$-ratio of average fluorescence intensity with doxycycline (D2Zy) relative to no doxycycline (D0Zy). Bottom panel: $\log_{10}$-ratio of fitness with zeocin (DxZ2) relative to no zeocin (DxZ0), either with or without doxycycline ($x = 0$ or $x = 2$). Error bars and stars as in (A).

D Phenotype of the single clone isolated from intermediate doxycycline and antibiotic zeocin (DiZ2, "suboptimal response"). The bars marked "A." correspond to the ancestral PF cells, and the other bars correspond to the mutant clone. Top panel: $\log_{10}$-ratio of fitness with doxycycline (D2Zy) relative to no doxycycline (D0Zy) either with or without zeocin ($y = 0$ or $y = 2$). Middle panel: $\log_{10}$-ratio of average fluorescence intensity with doxycycline (D2Zy) relative to no doxycycline (D0Zy). Bottom panel: $\log_{10}$-ratio of fitness with zeocin (DxZ2) relative to no zeocin (DxZ0), either with or without doxycycline ($x = 0$ or $x = 2$). Error bars and stars as in (A).

E Gene expression histograms measured in D0Z0 for Clones #4 and #7 (evolved in D0Z2) compared to the PF ancestor (shaded histogram).

F Gene expression histograms measured in DiZ2 for Clone #1 (evolved in DiZ2) compared to the PF ancestor (shaded histogram).

G Tradeoff between yEGFP::zeoR expression and zeocin resistance for clones evolved in D0Z2 (red) and DiZ2 (green).

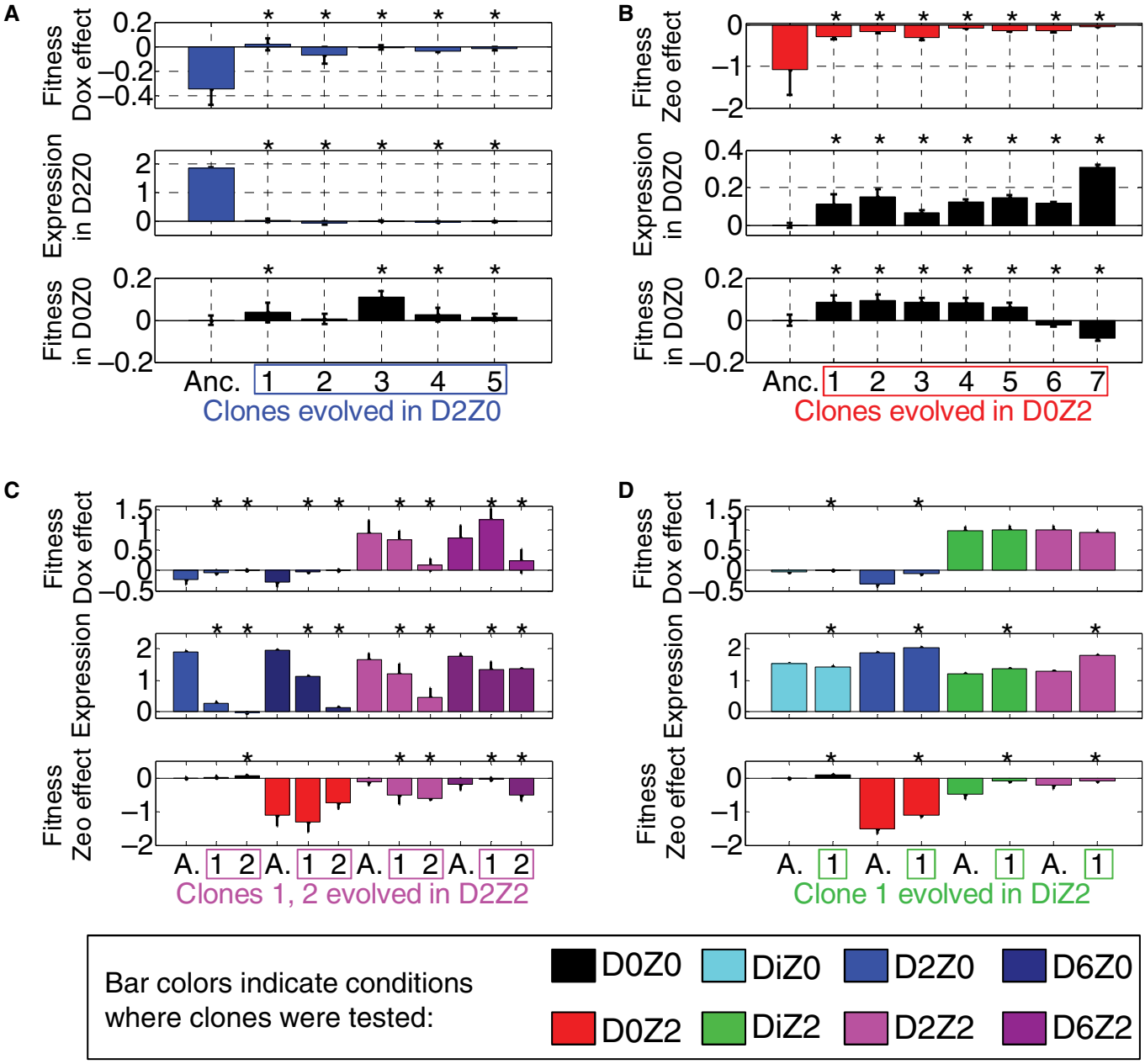
A
Fitness Dox effect
Expression in D2Z0
Fitness in D0Z0
Anc. 1 2 3 4 5
Clones evolved in D2Z0
B
Fitness Zeo effect
Expression in D0Z0
Fitness in D0Z0
Anc. 1 2 3 4 5 6 7
Clones evolved in D0Z2
C
Fitness Dox effect
Expression
Fitness Zeo effect
A. 1 2 A. 1 2 A. 1 2 A. 1 2
Clones 1, 2 evolved in D2Z2
D
Fitness Dox effect
Expression
Fitness Zeo effect
A. 1 A. 1 A. 1 A. 1
Clone 1 evolved in DiZ2
Bar colors indicate conditions where clones were tested:
D0Z0
DiZ0
D2Z0
D6Z0
D0Z2
DiZ2
D2Z2
D6Z2

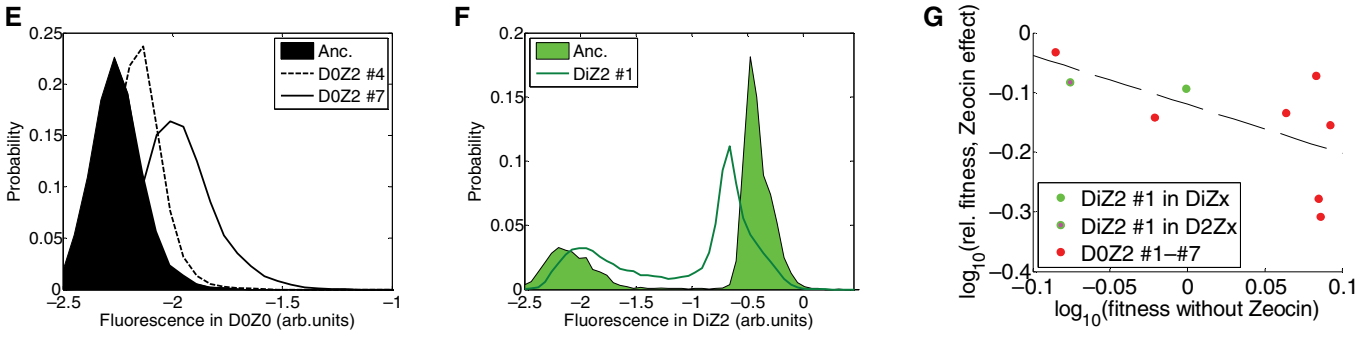
E
Anc.
D0Z2 #4
D0Z2 #7
Probability
Fluorescence in D0Z0 (arb.units)
F
Anc.
DiZ2 #1
Probability
Fluorescence in DiZ2 (arb.units)
G
log10(rel. fitness, Zeocin effect)
DiZ2 #1 in DiZx
DiZ2 #1 in D2Zx
D0Z2 #1–#7
log10(fitness without Zeocin)

Figure 6.

Additional insights into PF evolutionary dynamics

Experimental evolution and phenotyping validated the major mutation types predicted computationally for each condition. Therefore, we asked whether the computational framework could provide any additional insights into evolutionary forces and mechanisms based on the experimental data.

First, we tried to estimate the rate μ of potentially beneficial mutations using its predicted effect on various allele numbers in several conditions. Interestingly, we could not capture the experimental number of alleles and the half-life of ancestral genotype when we applied the same mutation rate in all conditions. Instead, comparing the results of computational simulations (Fig 4C; Appendix Fig S2D and F) with experimental data suggested slightly higher mutation rate in zeocin than without it (Fig 2). Specifically, the rate of potentially beneficial mutations that matched the data best was $\mu_{-Z} = 10^{-6.2}$ with zeocin compared to $\mu_{+Z} = 10^{-5.4}$/genome/generation without zeocin. This increase is reasonable because zeocin is a DNA-damaging agent that may elevate mutation rates. These beneficial mutation rates are comparable with a recent estimate in yeast of ~10^{-6}/genome/generation (Levy *et al*, 2015).

Second, we asked whether we could extract any information about the mutation probabilities P(K), P(T), and P(G). We compared simulation results with experimental data in D2Z0 and D2Z2 conditions where K- and T-type mutations should be prevalent, respectively. Selection for various mutation types is environment-dependent, implying that the number and type of established mutations must depend on the K/T bias in mutations entering the population. For example, while mainly T-type mutations can establish and the K-type is deleterious in D2Z2 (since it forces cells into the drug-sensitive Off state), the opposite is true in D2Z0. Comparing experimentally observed allele numbers with simulation results indicated that incoming T mutations should be in the minority (gray bars, Fig 2B and C) compared to the ~10 times more available K-type mutations. This suggests that only a few, specific rtTA loci can harbor T-type mutations, explaining recurrence of certain mutations in D2Z2. These recurrent mutations must have the rare capability of tweaking protein function and toxicity while still maintaining drug resistance, as predicted computationally and validated experimentally (Fig 6).

Finally, we asked how mutations that arose prior to setting the environmental conditions may have contributed to the outcome of evolution experiments. This was important because the PF cells grew for 24 h in D0Z0 before initiating our evolution experiments. To address this question, we used a variant of the simulation framework that allowed neutral mutations to accumulate for 24 h of growth at the mutation rate $\mu_{-Z} = 10^{-6.2}$/genome/generation. Afterward, we changed the simulated condition to DiZ0, D2Z0, DiZ2, D2Z2, or D0Z2 using values of the free parameters estimated from experimental data. We then computed the contribution of these "preexisting" mutations to the final allele frequencies (Appendix Fig S8). The results indicated that preexisting mutations do not comprise a large fraction of mutant alleles in conditions DiZ0, D2Z2, and DiZ2. On the other hand, in steep monotonic cellular fitness landscapes (D2Z0 and D0Z2), preexisting alleles could comprise approximately 35% of mutant alleles in D2Z0 and ~50% in D0Z2. Nevertheless, the same mutation types dominated in specific conditions with or without pre-existing mutations. Likewise, the pre-existing mutations did not substantially alter the ancestral genotype's half-life in any condition (Appendix Fig S8).

Discussion

Stress response networks play key roles in the emergence of drug resistance, from pathogenic microbes to cancer. Typically, stress response incorporates a tradeoff: cells that activate it grow slower in the absence of stress. Therefore, optimality of these networks depends on maintaining the balance between environmental stress and internal response. Yet, it is unknown how quickly, how reproducibly, and through what types of mutations stress response networks evolve to balance the costs and benefits of their response to external stress. What aspects of network evolution are predictable *a priori* and what is required for making predictions is unclear. To address these questions, we studied evolving yeast cells endowed with a synthetic stress response gene circuit that allowed for separate control of the stress and the response by adjusting antibiotic and inducer concentrations, respectively.

Using quantitative knowledge of the PF gene circuit, we developed two computational models to predict specific aspects of evolutionary dynamics in six different environmental conditions. The predicted aspects included the speed at which the ancestral genotype disappears from the population, as well as the types and numbers of mutant alleles that establish in each environmental condition. We validated these predictions by experimental evolution. The agreement between our predictions and experimental findings suggests that cellular and population fitness landscapes can be useful to predict short-term evolution. Critically, our predictive models were based on quantitative knowledge of the fitness and gene expression properties, as well as the genetic structure (design) of the PF gene circuit. Without such knowledge, it would have been impossible to predict what type of mutations arise and how fast. Once this knowledge is acquired, however, cellular and population fitness landscapes (Fig 1B) can be constructed, which are informative for predicting evolutionary outcomes.

We found a connection between the rates at which various potentially beneficial mutations entered the populations and the computationally predicted features of evolutionary dynamics, especially the number of mutant alleles (Appendix Fig S3). This allowed a rough estimation of the relative probabilities of two mutation types to occur spontaneously. We found that mutations eliminating protein function were much more common than mutations fine-tuning protein function (at least for rtTA in these experiments). The availability of various beneficial mutation types depends on DNA sequence and is rarely known *a priori*. We suggest nonetheless that the availability of mutation types could be estimated by comparing computational predictions with actual observations in similar laboratory evolution experiments.

A unifying theme for all environmental conditions was the tradeoff between stress resistance and stress-free growth: genotypes that resisted zeocin tended to grow slower in its absence. Such tradeoffs were inherent by design to the ancestral PF synthetic gene circuit (Fig 1B). However, in D0Z2, yeast adapted using extra-PF mutations that were not subject to the original tradeoff. Most surprisingly, these extra-circuit changes were subject to a different tradeoff,

which resembled the original one in the PF gene circuit (Fig 6G). Essentially, there was a cost for higher yEGFP::zeoR expression, even if caused by extra-circuit mutations. Thus, without the built-in tradeoff within the PF gene circuit, another tradeoff appears through mutations outside of the PF gene circuit. This suggests a fundamental conflict between two different tasks (resistance to stress and fast growth in stress-free conditions), typically resolved by Pareto optimization (Shoval *et al*, 2012). Such "multi-layered" tradeoffs (when multiple ways of coping with stress exist, but each has its own type of tradeoff) may occur frequently in many natural systems, including more complex genetic circuits in other organisms.

The ultimate success of synthetic biology will depend on the long-term practical applicability of synthetic constructs. Despite the growing number of synthetic constructs, their evolutionary stability only recently began to be investigated in *Escherichia coli* (Yokobayashi *et al*, 2002; Sleight *et al*, 2010; Wu *et al*, 2014). As far as we know, this question has not been addressed in eukaryotes. Our work fills this gap and generates insights for building evolutionarily robust eukaryotic gene circuits. The PF gene circuit is based on the rtTA activator, which is widely utilized in eukaryotic synthetic biology. An important insight that we gained was that eukaryotic activators like rtTA are not ideal if gene circuit stability is a concern. There is evidence that eukaryotic activators are generally toxic (Baron *et al*, 1997), which seems to be true for some prokaryotic components as well (Tan *et al*, 2009). To address this problem, some groups have tried to identify eukaryotic activators with reduced toxicity (Baron *et al*, 1997; Khalil *et al*, 2012). Still, we would recommend avoiding long-term use of common eukaryotic activators (utilizing VP16, VP64, or GAL activator domains, including in dCas9-, TALE-, or zinc finger-based synthetic regulators) until their genetic stability has been carefully tested in long-term evolution experiments. Our experiments could be considered as testing rtTA activator stability in various environments. The experiments revealed the evolutionary instability of rtTA, but also led to the discovery of mutant activators and gene circuit designs with lower activator toxicity. These could become novel parts and designs minimizing activator toxicity when eukaryotic activators are needed, as in memory circuits (Ajo-Franklin *et al*, 2007; Burrill *et al*, 2012).

To conclude, this work highlights the unique ability of synthetic biological constructs to provide improved, quantitative understanding and predictability to fundamental biological processes such as evolution and development. Similar studies will be essential to assess and improve the evolutionary stability of synthetic gene circuits, enabling their industrial and clinical application. Therefore, synthetic biology is about to reverse the information flow toward other fields of biology, the source of original inspiration for parts and concepts for the first synthetic genetic constructs.

Materials and Methods

Strains and media

We used the haploid *Saccharomyces cerevisiae* strain YPH500 (α, *ura3-52*, *lys2-801*, *ade2-101*, *trp1Δ63*, *his3Δ200*, *leu2Δ1*; Stratagene, La Jolla, CA) with the PF synthetic gene circuit stably integrated into chromosome XV near the *HIS3* locus as described previously (Nevozhay *et al*, 2012). Cultures were grown in synthetic dropout (SD) medium with 2% weight of sugar (glucose or galactose) and the appropriate supplements (*-his*, *-trp*) to maintain auxotrophic selection (reagents from Sigma, St. Louis, MO).

Experimental evolution

In preparation for the experiments, the PF ancestor strain was streaked on SD 2% glucose plates. Plates were incubated at 30°C for 2 days. Well-isolated single colonies were picked into 1 ml SD-*his-trp* 2% galactose liquid medium and incubated overnight at 30°C with orbital shaking at 250 rpm and resuspended regularly (every 12 h or every 24 h). Fluorescence and cell density measurements were taken daily or every 12 h. Samples were saved daily and stored in 80% glycerol at −80°C for further studies. Further details are described in the Appendix.

Fitness landscape mapping and parameter estimation

Ancestral PF cells were prepared as described above. Cultures were then resuspended into the following treatments: zeocin only (0.5, 1.0, 1.5 and 2.0 mg/ml), doxycycline only (0.2, 0.5, 1 and 2 μg/ml), and both doxycycline (0.2, 0.5, 1 and 2 μg/ml) and zeocin (2 mg/ml). Cell density and fluorescence were measured every 6 h over 72 h.

Population and cellular growth rates were estimated using mathematical models described previously (Nevozhay *et al*, 2012) and as described in the Appendix. Briefly, we used fitness functions to model the effects of conditions and gene expression on growth. One depends on zeocin and yEGFP::ZeoR protein concentration: $\gamma_1 = \frac{\chi}{\chi + z_i(F,Z)}$ where Z_i is inferred from the steady-state solution of a dynamical model:

$$\dot{Z}_i = \phi Z - h_z Z_i - sRZ_i$$
$$\dot{B} = sRZ_i - dB$$

with Z, B, and R representing external zeocin, and bound and unbound yEGFP::ZeoR protein concentrations ($F = B + R$). The other depends on doxycycline and yEGFP::ZeoR protein concentration, assumed to be equal with rtTA protein concentration: $\gamma_2 = g_0 \frac{\alpha}{\alpha + F\frac{C}{C+\beta}}$ with C representing doxycycline concentration. The total growth rate is then $\gamma = \gamma_1\gamma_2$.

In each condition, the rate of switching from low to high expression and vice versa (cellular memory) was inferred from experimental dose responses in doxycycline as described previously (Nevozhay *et al*, 2012; Appendix Fig S3E).

Resulting parameter estimates are presented in Appendix Table S1.

Statistical analysis of gene expression and fitness data

Fluorescence and fitness values were compared using *t*-tests in our study. We used an "independent samples" version of the *t*-test to compare different conditions (for example, D0Z0 and D0Z2). On the other hand, we used a dependent (paired) samples version of the *t*-test to compare different time points within one environmental condition. We applied Bonferroni correction for multiple comparisons whenever applicable. All tests were performed in STATISTICA 9.1 (StatSoft Inc., Tulsa, OK).

Gene expression and fitness characterization of clonal isolates (phenotyping)

Fitness of clones isolated from evolved populations was estimated using an Infinite M200 Pro plate reader (Tecan) for OD_{600} measurements (600 ± 9 nm, number of reads = 25) of orbitally shaken (280.8 rpm with amplitude 2 mm) 250 µl cultures in 96-well plates at 30 ± 0.5°C. Cultures were rediluted into fresh media of identical composition every 12 h. Fluorescence was measured every 24 h by flow cytometry.

Mathematical and computational models

We have developed two different types of predictive models. The first model was a set of ordinary differential equations (ODEs) with the number of ancestral cells, and mutants lumped into K, T, G categories as variables, assuming constant population size. A detailed description of the model is in the Appendix.

The second model was an evolutionary simulation framework explicitly accounting for each individual mutation over the time course written in Python 3. In the framework, we used a linear system of ordinary differential equations (ODEs) to describe ancestral and mutant cells, with experimentally inferred growth rates (g_L, g_H) and switching rates (r, f). The simulation framework includes population growth, zeocin internalization dynamics, entry of mutation types K, T, or G into the population and simulated 12-h resuspensions (Appendix Fig S1B and C). We simulated all of the experimental conditions with appropriate growth and switching parameters. To test the effect of preexisting mutations, we simulated a 24-h period without selection before changing the parameters to those appropriate for each condition. The simulation framework is described in greater detail in the Appendix along with its Python script.

The rates of switching, growth, and zeocin internalization were all determined experimentally prior to the simulations (Appendix Table S1). Thus, the three free parameters in each condition were beneficial mutation rate (µ), and the relative probabilities of a mutation being of type K, or T. These parameters were systematically scanned in both models to determine the robustness of our predictions.

Mutation time course reconstruction

We reconstructed time courses of mutation frequencies for experimental evolution replicates D2Z0-12 h-1 (Fig 3D), DiZ0-12 h-1 (Fig 3E), D0Z2-12 h-1 (Fig 4B), D2Z2-12 h-1 (Fig 5D), DiZ2-12 h-1 (Fig 5E), D2Z0-24 h-1 (Appendix Fig S4B), D0Z2-24 h-1 (Fig 4B, Appendix Fig S5B), and D2Z2-24 h-1 (Appendix Fig S6B). In each case, we had allele frequencies inferred from either Sanger sequencing alone, whole-genome Illumina sequencing alone, or both. For time points with allele frequency data from both methods, we plotted the mean of frequencies between the methods. If only one sequencing method was applied for a given time point, we used the corresponding inferred allele frequency. The number of sequenced time points varied between 2 and 6 depending on the condition (excluding $t = 0$ h; gray points). Once the ancestral genotype reached 0%, we kept it at 0% (even if in rare cases mutant alleles could not account for 100% of the population afterward).

In many conditions, we observed multiple mutations in the same sample. To obtain information on linkage, we performed Sanger sequencing on clonal isolates, at mutation loci determined by whole-genome Illumina sequencing. When linked mutations were called, we averaged the whole-genome frequency estimates of the two mutants to approximate the linked allele frequency. We then averaged that value with frequency estimates from Sanger sequencing. This method permitted inference of linked-mutant frequencies at time points that used both sequencing methods. For example, Appendix Fig S4B shows just the whole-genome inferred allele frequencies for all whole-genome-sequenced time points with no linkage data (thus erroneously indicating lack of linkage for all detected alleles). To illustrate the likely course of allele dynamics at times between the measured points, we used second-order spline interpolation (gray lines).

Expanded View for this article is available online:
http://msb.embopress.org

Acknowledgements
This research was supported by the NIH Director's New Innovator Award Program (1DP2 OD006481-01), by NSF/IOS 1021675 and the Laufer Center for Physical & Quantitative Biology to GB and an Alfred P. Sloan Research Fellowship to AVM. DN acknowledges support from Program # 1326 of the Ministry of Education and Science, Russian Federation, and CG acknowledges support from the Division of Academic Affairs at the MD Anderson Cancer. Sequencing was performed at MD Anderson's DNA Analysis core facility (funded by NCI CA16672). We would like to thank the organizers and participants of the NSF-supported (Grant #1066293) Aspen Center for Physics workshop "Evolutionary Dynamics and Information Hierarchies in Biological Systems" (2012) and the NSF-supported (Grant #PHY11-25915) "Cooperation and the Evolution of Multicellularity" workshop (2013, Kavli Institute for Theoretical Physics) for discussions. MM would like to thank Bill Flynn and Ariella Sasson for assistance with sequencing data analysis. We thank J. Xavier, M. Rosner, D. Charlebois, M. Szenk, T. Székely, S. Levy and J. J. Collins for comments and discussions. We also thank two anonymous reviewers for their highly insightful and constructive comments.

Author contributions
CG, JCJR, MM, RMA, DN, AVM, and GB designed research; CG and DN performed experiments; CG, JCJR, MM, RMA, DN, and GB analyzed the data; CG, JCJR, MM, RMA, DN, AVM, and GB developed computational models; and CG, JCJR, MM, RMA, DN, AVM, and GB wrote the paper.

Conflict of interest
The authors declare that they have no conflict of interest.

References

Ajo-Franklin CM, Drubin DA, Eskin JA, Gee EP, Landgraf D, Phillips I, Silver PA (2007) Rational design of memory in eukaryotic cells. *Genes Dev* 21: 2271 – 2276

Andersson DI, Levin BR (1999) The biological cost of antibiotic resistance. *Curr Opin Microbiol* 2: 489 – 493

Balaban NQ, Merrin J, Chait R, Kowalik L, Leibler S (2004) Bacterial persistence as a phenotypic switch. *Science* 305: 1622 – 1625

Balázsi G, van Oudenaarden A, Collins JJ (2011) Cellular decision making and biological noise: from microbes to mammals. *Cell* 144: 910 – 925

Baron U, Gossen M, Bujard H (1997) Tetracycline-controlled transcription in eukaryotes: novel transactivators with graded transactivation potential. *Nucleic Acids Res* 25: 2723 – 2729

Beaumont HJ, Gallie J, Kost C, Ferguson GC, Rainey PB (2009) Experimental evolution of bet hedging. *Nature* 462: 90 – 93

Becskei A, Seraphin B, Serrano L (2001) Positive feedback in eukaryotic gene networks: cell differentiation by graded to binary response conversion. *EMBO J* 20: 2528 – 2535

Burger RM (1998) Cleavage of nucleic acids by bleomycin. *Chem Rev* 98: 1153 – 1169

Burrill DR, Inniss MC, Boyle PM, Silver PA (2012) Synthetic memory circuits for tracking human cell fate. *Genes Dev* 26: 1486 – 1497

Charlebois DA, Abdennur N, Kaern M (2011) Gene expression noise facilitates adaptation and drug resistance independently of mutation. *Phys Rev Lett* 107: 218101

Dekel E, Alon U (2005) Optimality and evolutionary tuning of the expression level of a protein. *Nature* 436: 588 – 592

van Ditmarsch D, Boyle KE, Sakhtah H, Oyler JE, Nadell CD, Deziel E, Dietrich LE, Xavier JB (2013) Convergent evolution of hyperswarming leads to impaired biofilm formation in pathogenic bacteria. *Cell Rep* 4: 697 – 708

Elowitz MB, Leibler S (2000) A synthetic oscillatory network of transcriptional regulators. *Nature* 403: 335 – 338

Gardner TS, Cantor CR, Collins JJ (2000) Construction of a genetic toggle switch in Escherichia coli. *Nature* 403: 339 – 342

Gari E, Piedrafita L, Aldea M, Herrero E (1997) A set of vectors with a tetracycline-regulatable promoter system for modulated gene expression in *Saccharomyces cerevisiae*. *Yeast* 13: 837 – 848

Gasch AP, Spellman PT, Kao CM, Carmel-Harel O, Eisen MB, Storz G, Botstein D, Brown PO (2000) Genomic expression programs in the response of yeast cells to environmental changes. *Mol Biol Cell* 11: 4241 – 4257

Gatignol A, Durand H, Tiraby G (1988) Bleomycin resistance conferred by a drug-binding protein. *FEBS Lett* 230: 171 – 175

Hillen W, Berens C (1994) Mechanisms underlying expression of Tn10 encoded tetracycline resistance. *Annu Rev Microbiol* 48: 345 – 369

Hsieh AC, Moasser MM (2007) Targeting HER proteins in cancer therapy and the role of the non-target HER3. *Br J Cancer* 97: 453 – 457

Hsu C, Scherrer S, Buetti-Dinh A, Ratna P, Pizzolato J, Jaquet V, Becskei A (2012) Stochastic signalling rewires the interaction map of a multiple feedback network during yeast evolution. *Nat Commun* 3: 682

Kashtan N, Alon U (2005) Spontaneous evolution of modularity and network motifs. *Proc Natl Acad Sci USA* 102: 13773 – 13778

Kauffman S (1993) *Origins of Order: Self-Organization and Selection in Evolution*. New York, NY: Oxford University Press

Khalil AS, Lu TK, Bashor CJ, Ramirez CL, Pyenson NC, Joung JK, Collins JJ (2012) A synthetic biology framework for programming eukaryotic transcription functions. *Cell* 150: 647 – 658

Lang GI, Rice DP, Hickman MJ, Sodergren E, Weinstock GM, Botstein D, Desai MM (2013) Pervasive genetic hitchhiking and clonal interference in forty evolving yeast populations. *Nature* 500: 571 – 574

Lenski RE, Travisano M (1994) Dynamics of adaptation and diversification: a 10,000-generation experiment with bacterial populations. *Proc Natl Acad Sci USA* 91: 6808 – 6814

Levy SF, Ziv N, Siegal ML (2012) Bet hedging in yeast by heterogeneous, age-correlated expression of a stress protectant. *PLoS Biol* 10: e1001325

Levy SF, Blundell JR, Venkataram S, Petrov DA, Fisher DS, Sherlock G (2015) Quantitative evolutionary dynamics using high-resolution lineage tracking. *Nature* 519: 181 – 186

Lobkovsky AE, Koonin EV (2012) Replaying the tape of life: quantification of the predictability of evolution. *Front Genet* 3: 246

Lopez-Maury L, Marguerat S, Bahler J (2008) Tuning gene expression to changing environments: from rapid responses to evolutionary adaptation. *Nat Rev Genet* 9: 583 – 593

Mason J, Linsay PS, Collins JJ, Glass L (2004) Evolving complex dynamics in electronic models of genetic networks. *Chaos* 14: 707 – 715

Maynard ND, Birch EW, Sanghvi JC, Chen L, Gutschow MV, Covert MW (2010) A forward-genetic screen and dynamic analysis of lambda phage host-dependencies reveals an extensive interaction network and a new anti-viral strategy. *PLoS Genet* 6: e1001017

Moon TS, Lou C, Tamsir A, Stanton BC, Voigt CA (2012) Genetic programs constructed from layered logic gates in single cells. *Nature* 491: 249 – 253

Munsky B, Neuert G, van Oudenaarden A (2012) Using gene expression noise to understand gene regulation. *Science* 336: 183 – 187

Nevozhay D, Adams RM, Van Itallie E, Bennett MR, Balázsi G (2012) Mapping the environmental fitness landscape of a synthetic gene circuit. *PLoS Comput Biol* 8: e1002480

Nevozhay D, Zal T, Balázsi G (2013) Transferring a synthetic gene circuit from yeast to mammalian cells. *Nat Commun* 4: 1451

New AM, Cerulus B, Govers SK, Perez-Samper G, Zhu B, Boogmans S, Xavier JB, Verstrepen KJ (2014) Different levels of catabolite repression optimize growth in stable and variable environments. *PLoS Biol* 12: e1001764

Poelwijk FJ, de Vos MGJ, Tans SJ (2011) Tradeoffs and optimality in the evolution of gene regulation. *Cell* 146: 462 – 470

Purnick PE, Weiss R (2009) The second wave of synthetic biology: from modules to systems. *Nat Rev Mol Cell Biol* 10: 410 – 422

Quan S, Ray JCJ, Kwota Z, Duong T, Balázsi G, Cooper TF, Monds RD (2012) Adaptive evolution of the lactose utilization network in experimentally evolved populations of *Escherichia coli*. *PLoS Genet* 8: e1002444

Sanchez A, Golding I (2013) Genetic determinants and cellular constraints in noisy gene expression. *Science* 342: 1188 – 1193

Shoval O, Sheftel H, Shinar G, Hart Y, Ramote O, Mayo A, Dekel E, Kavanagh K, Alon U (2012) Evolutionary trade-offs, pareto optimality, and the geometry of phenotype space. *Science* 336: 1157 – 1160

Sleight SC, Bartley BA, Lieviant JA, Sauro HM (2010) Designing and engineering evolutionary robust genetic circuits. *J Biol Eng* 4: 12

Stricker J, Cookson S, Bennett MR, Mather WH, Tsimring LS, Hasty J (2008) A fast, robust and tunable synthetic gene oscillator. *Nature* 456: 516 – 519

Sumner ER, Avery SV (2002) Phenotypic heterogeneity: differential stress resistance among individual cells of the yeast *Saccharomyces cerevisiae*. *Microbiology* 148: 345 – 351

Tan C, Marguet P, You L (2009) Emergent bistability by a growth-modulating positive feedback circuit. *Nat Chem Biol* 5: 842 – 848

Tanouchi Y, Pai A, Buchler NE, You L (2012a) Programming stress-induced altruistic death in engineered bacteria. *Mol Syst Biol* 8: 626

Tanouchi Y, Smith RP, You L (2012b) Engineering microbial systems to explore ecological and evolutionary dynamics. *Curr Opin Biotechnol* 23: 791 – 797

Tenaillon O, Rodriguez-Verdugo A, Gaut RL, McDonald P, Bennett AF, Long AD, Gaut BS (2012) The molecular diversity of adaptive convergence. *Science* 335: 457 – 461

Thattai M, van Oudenaarden A (2004) Stochastic gene expression in fluctuating environments. *Genetics* 167: 523 – 530

Toprak E, Veres A, Michel JB, Chait R, Hartl DL, Kishony R (2012) Evolutionary paths to antibiotic resistance under dynamically sustained drug selection. *Nat Genet* 44: 101 – 105

Urlinger S, Baron U, Thellmann M, Hasan MT, Bujard H, Hillen W (2000) Exploring the sequence space for tetracycline-dependent transcriptional activators: novel mutations yield expanded range and sensitivity. *Proc Natl Acad Sci USA* 97: 7963 – 7968

Wang YH, Arenas CD, Stoebel DM, Cooper TF (2013) Genetic background affects epistatic interactions between two beneficial mutations. *Biol Lett* 9: 20120328

Wishart JA, Hayes A, Wardleworth L, Zhang NS, Oliver SG (2005) Doxycycline, the drug used to control the tet-regulatable promoter system, has no effect on global gene expression in Saccharomyces cerevisiae. *Yeast* 22: 565 – 569

Wu F, Menn DJ, Wang X (2014) Quorum-sensing crosstalk-driven synthetic circuits: from unimodality to trimodality. *Chem Biol* 21: 1629 – 1638

Yamaguchi Y, Park JH, Inouye M (2011) Toxin-antitoxin systems in bacteria and archaea. *Annu Rev Genet* 45: 61 – 79

Yokobayashi Y, Weiss R, Arnold FH (2002) Directed evolution of a genetic circuit. *Proc Natl Acad Sci USA* 99: 16587 – 16591

Appendix

Stress-response balance drives the evolution of a network module and its host genome

Caleb González[1*], J. Christian J. Ray[1,2,*], Michael Manhart[3,4], Rhys M. Adams[1], Dmitry Nevozhay[1,5], Alexandre V. Morozov[3,6], and Gábor Balázsi[1,7,8,‡]

[1]Department of Systems Biology - Unit 950, The University of Texas MD Anderson Cancer Center, Houston, TX 77054, USA

[2]Center for Computational Biology & Department of Molecular Biosciences, University of Kansas, Lawrence, KS 66045, USA

[3]Department of Physics & Astronomy, Rutgers University, Piscataway, NJ 08854, USA

[4]Department of Chemistry and Chemical Biology, Harvard University, Cambridge, MA 02138, USA

[5]School of Biomedicine, Far Eastern Federal University, 8 Sukhanova Street, Vladivostok, 690950, Russia

[6]BioMaPS Institute for Quantitative Biology, Rutgers University, Piscataway, NJ 08854, USA

[7]Laufer Center for Physical & Quantitative Biology, Stony Brook University, Stony Brook, NY 11794, USA

[8]Department of Biomedical Engineering, Stony Brook University, Stony Brook, NY 11794, USA

[*]Equal contribution

Table of Contents

1. Evolution experiments and sequencing: Experimental procedures

1.1. 12-hour resuspension experiments

We started by determining the cell concentration of overnight cultures. Then we diluted the cells to 10^6 cells/mL and inoculated them into six different treatments based on SD-*his-trp* medium with 2% galactose: D0Z0 consisting of neither Doxycycline nor Zeocin; D2Z0 consisting of Doxycycline only (2 μg/mL; Acros Organics, Geel, *Belgium*); DiZ0 consisting of 0.2 μg/mL Doxycycline only; D0Z2 consisting of only Zeocin (2 mg/mL; Invitrogen, Carlsbad, CA); D2Z2 consisting of 2 μg/mL Doxycycline and 2 mg/mL Zeocin; and DiZ2 consisting of 0.2 μg/mL Doxycycline and 2 mg/mL Zeocin. 10^6 cells were then resuspended similarly into their respective treatments every 12 hours for ~3 weeks. Cell density was measured (Nexcelom M10) every 12 hours and fluorescence was measured by flow cytometry every 24 hours. Malthusian fitness between subsequent resuspensions was estimated by a linear fit to log-transformed total cell counts (inferred from cell density and culture volume): $g = \frac{1}{12}\ln\left(\frac{N_{12}}{N_0}\right)$. Samples were saved daily and stored in 80% glycerol at -80°C for further studies.

1.2. 24-hour resuspension experiments

Overnight cultures were diluted 100-fold, divided into 3 replicates, each inoculated into four different treatments: D0Z0, D0Z2, D2Z0, and D2Z2, as described above. Cultures were re-suspended daily into their respective treatments with appropriate dilutions aiming to start each time at 10^6 cells/mL. Cell density was measured daily on a Nexcelom M10 cell counter (Nexcelom Bioscience). The logistic growth equation $\frac{dN}{dt} = gN\left(1 - \frac{N}{N_{\max}}\right)$ was then used to estimate the Malthusian fitness $g = \frac{1}{24}\ln\left(\frac{N_{24}}{N_0} - \frac{N_{24}}{N_{\max}}\right) - \frac{1}{24}\ln\left(1 - \frac{N_{24}}{N_{\max}}\right)$ between subsequent resuspensions. Samples were saved daily and stored in 80% glycerol at -80°C for further studies.

1.3. Flow cytometry

Cultures were analyzed on a FACSAria II flow cytometer and sorter (BD Biosciences, San Jose, CA) using the 488nm blue excitation laser and 530/30 emission filter for EGFP. Raw flow cytometry data files were read into MATLAB (Mathworks, Inc.) using the Matlab script fca_readfcs (MATLAB Central) for plotting and analysis. We divided the fluorescence intensity (FL1) by (FSC)¾ for an approximate normalization by cell volume to approximate yEGFP concentrations, minimizing cell-cycle and cell size biases. The unnormalized data was very similar, except the distributions were generally broader.

1.4. Whole-genome sequencing

Samples taken directly from the -80°C collection were inoculated into the same treatment in which the cells evolved. After overnight shaking at 30°C, whole-genome extractions were performed with the DNeasy Blood & Tissue Kit (Qiagen) using the supplier's protocol modified for yeast. Genomic

extracts were treated with 2 μg of RNAse (Qiagen) for 75 minutes at 37°C. Samples were then whole-genome sequenced at MD Anderson's Sequencing and Microarray Facility on a HiSeq2000 Sequencer (Illumina Inc.). The average coverage genome-wide was ~100. Allele frequencies were inferred as: $N_{(\text{reads with the allele})}/N_{(\text{total reads at that locus})}$.

1.5. Sanger sequencing

Samples were streaked on plates as described. Ten to twelve single well-isolated colonies were picked and incubated overnight shaking at 30°C in 1.5 mL SD-*his-trp* medium. The following day 0.5 mL of overnight culture was saved in 80% glycerol at -80°C for further studies. The remaining 1 mL of overnight culture was used for genomic extractions as described above. Sanger sequencing was performed on a Seqwright DNA sequencer (GE Healthcare / Seqwright Genomic Services, Houston, TX), utilizing specific primers that targeted the region of interest (primer list below). Sequences were aligned to the reference sequence and analyzed using the SEQMAN PRO software (DNASTAR®, Lasergene). Sequencing primers were designed to target the genetic sequence with at least double coverage, and mutation calls were confirmed with at least two different shotgun sequences resulting from the respective primers. Allele frequencies were inferred as: $N_{(\text{colonies with allele})}/N_{(\text{total colonies})}$.

1.6. Primers used for sequencing extra-circuit mutations

Name	Sequence
Gal2-1-Seq-f	GGTTTAATCGTCGCCATTTTCA
Gal2-1-Seq-r	GGAACTAACGTCAAAGCGCC
GAL2-Seq-f	ATGGCCGTAAAAAGGGTCTTTCGATTGTCG
GAL2-Seq-r	GGAGGCAAAGTTGACTACACCAATGACAATG
EOS1-Seq-f	GCAAGAGCGTCTGAATATCT
EOS1-Seq-r	CTGTCGTTGGAAGGAACATC
MLH3-f	GCGCTCGCAAATAAACGCAAACTAAATATAAGCG
MLH3-r	GTTAGTCTCTGCTGAACATCAATCTCAGATGATTC
STB3-Seq-f	TAATGTGTCTAATGGCCAATGGTCCCATTTC
STB3-Seq-r	GATTATAAAAGACACTGATTGCAAACGGTGC
YDR186c -Seq-f	TGTCATTTAATAATTTGGAAAATGCGTTTG
YDR186c -Seq-r	ACGATGAAGGTTTGAGCTTTTACGCTCCAAGC
INO2-Seq-f	CTGCTGAGCATTTGGTAAGCAGTTTCAAAG
INO2-Seq-r	AACCACACTCAAACCAAATCTACGCCAGCTAC
RPS0A-Seq-f	GGTTTAATCTGGTACTTATTGGCTAGAGAAG
RPS0A-Seq-r	TTTAGATCACTATATACGCTACGTGTTGATAAG
SRX1-Seq-f	AGCCTTTGGCCTCTGCAATACTAGCGATTGC
SRX1-Seq-r	GCCTGTTCTAGAGAGCATGTCTTGCTAGCGG
RPL9B-Seq-f	ATCGTCAAGGTTGTCGGTCCAAGAGGTACTTTG
RPL9B-Seq-r	GTCTTCGACAATGAAACCCTTGTGGGAAACG
GUP2-Seq-f	ACTTACGCGCCATTGTTTTTAGTGGGCCCAATTATCAC
GUP2-Seq-r	TTGGATGTCATGCCATATTGCTACAAATGAGAATAC

1.7. Primers used for sequencing the rtTA (regulator) region

rtTA amplifying primers:

Name	Sequence
TRP-f	ATGTCTGTTATTAATTTCACAGGTAGTTC
DED1-r	TCCATCTACCACCAGAACGGCCGTTAGATC

rtTA sequencing primers:

Name	Sequence
rtTA-seq-int-r-cg	CGACTTGATGCTCTTGTTCTTCCAATACGCAACC
rtTA-seq-int-f-cg	GCCAACAAGGTTTTTCACTAGAGAATGCATTATATG
Tetreg-AflII-f	GCGCCTTAAGGCGCCACTTCTAAATAAGCGAATTTC
rtTABamHI2-f	GCGCGGATCCATGTCTAGATTAGATAAAAGTAAAG
FFF-XhoI-r	GCGCCTCGAGTTAACCTGGCAACATATCTAAATCAAAGTCATC TAATGCGTCGGCGGGTAGCATGTCTAGGTCGAAATCGTCAAGAGACA
Backbone-r	CGCGTTGGCCGATTCATTAATGC

1.8. Primers used for sequencing the yEGFP::zeoR (reporter) region

yEGFP::ZeoR amplifying primers:

Name	Sequence
His-f	ATGACAGAGCAGAAAGCCCTAGTAAAGC
Before2TRP-r	CACATATATTACGATGCTGTTCTATTAAATGCTTCC

yEGFP::ZeoR sequencing primers:

Name	Sequence
Backbone-r	CGCGTTGGCCGATTCATTAATGC
GalSeqE-r	TGAATAATTCTTCACCTTTAG
ZeoR-XhoI-r	gcgcctcgagTCAGTCCTGCTCCTC
yEGFP-BamHI-f	gcgcggatcctattaaaATGTCTAAAGGTGAAG
Origin-Middle-f	CTATTAAAGAACGTGGACTCCAACGTCAAAG
Tetreg-AflII-f	GCGCCTTAAGGCGCCACTTCTAAATAAGCGAATTTC

1.9. Primers used for reconstructing mutations in the ancestral genome

Mutation #1 in D2Z2 ($rtTA_{+225}$)

Name	Sequence
rtTA-mod1-f	GCCCTTTAGAAGGGGAAAGCTGCCAAGATTTTTTACGTAATAACGC
rtTA-mod1-r	GCGTTATTACGTAAAAAATCTTGGCAGCTTTCCCCTTCTAAAGGGC

Mutation #2 in D2Z2 ($rtTA_{-9}$)

Name	Sequence
Tetreg-AflII-f	GCGCCTTAAGGCGCCACTTCTAAATAAGCGAATTTC
Cyc1-BamHI_mod-r	GCGCGGATCCCCGGAATTGATCCGGTAATTTAGTG

2. Sequencing: Data analysis

2.1. Overview

We performed whole-genome sequencing with Illumnia HiSeq as described in the Experimental Procedures, obtaining 76-bp paired-end reads. We applied the following analysis pipeline:

1: Align reads (BWA/Bowtie 2)
2: Remove PCR duplicates (SAMtools)
3: Recalibrate base quality (GATK)
4: Calculate base alignment quality (SAMtools)
5: Call variants in each sample (FreeBayes)
6: Filter S288c/YPH500 strain differences
7: Match variants across time points
8: Manually validate in alignment (IGV)

We first aligned the raw reads to the S288c genome (*Saccharomyces* Genome Database, build R64-1-1) with the synthetic PF sequence inserted into chromosome XV (S288c+PF). To reduce biases from the alignment algorithm, we used both BWA-MEM (Li, 2013) and Bowtie 2 (Langmead & Salzberg, 2012) on default settings; we confirmed all reported mutations in both alignments, although for simplicity we only show the results from the BWA alignment.

We filtered the aligned reads for PCR duplicates using SAMtools (Li et al, 2009). We recalibrated raw base qualities from the sequencing instrument in two ways. First we recalibrated them in GATK (DePristo et al, 2011; McKenna et al, 2010) using a sample-specific error model accounting for biases in nucleotide and dinucleotide identity and position on the read. We then used SAMtools (Li et al, 2009) to cap the resulting base qualities by their read mapping quality ("base alignment quality") to suppress mismatches resulting from misalignments near short indels

We called SNPs using a heuristic filtering scheme implemented in FreeBayes (Garrison & Marth, 2012). For extra-PF variant calling, we filtered reads with Phred-scaled mapping quality less than 1 (to eliminate reads mapping to multiple locations) and bases with quality less than 10. We required putative variants to be supported by at least 2 reads and at least 5% of all reads covering that base; total coverage at the site is required to be greater than 30 (average coverage genome-wide is ~100). For variant calling within the PF sequence, we did not filter reads based on mapping quality because important parts of the PF sequence are repeated (e.g., the promoters for yEGFP::zeoR and rtTA), and because we could more easily assess possible alignment problems by hand. In all cases we also eliminated variants supported by reads mapping only to a single strand.

The above steps produced a list of putative variants for each sample. Most of these are likely due to systematic differences between the S288c genome and the genome of the YPH500 strain used in our experiments. To eliminate these, we only considered extra-PF variants that appeared in a single experiment (i.e., the same variant appearing in different experiments was presumed to be spurious) and at multiple time points within the same experiment. We also rejected variants in regions with dubious alignment (e.g., telomeres, transposons, long repeats). We did not apply these criteria to variants in the PF sequence. We also required all variants to be detected in both the BWA and Bowtie 2 alignments.

Finally, we manually validated all variants using the Integrative Genomics Viewer (Robinson et al, 2011; Thorvaldsdottir et al, 2013). **Appendix Tables S2-S5** list all such mutations passing these conditions.

2.2. Structural variant reconstruction and realignment

Sanger sequencing detected five larger structural variants (one 30-bp duplication, three 42-bp deletions, and one 78-bp deletion) in the synthetic PF sequence. Since our analysis pipeline for the whole-genome sequence data is not equipped to detect these, we attempted to confirm them in the whole-genome data by reconstructing the variants in the wild-type reference genome and then realigning the reads.

For the 30-bp tandem duplication detected in 24hr-D2Z0-r1 (**Appendix Table S3**), the alignment to the wild-type reference shows a clear signature of the duplication in the coverage profile (**Appendix Figure S4D**, top). As expected, when we aligned these same reads to a reference with the 30 bp duplication included, the coverage enhancement disappeared (**Appendix Figure S4D**, bottom). However, the reads did not align perfectly to this modified reference sequence because the duplication is only present in a fraction of the population.

In contrast to the tandem duplication, there was no clear signature of the three 42 bp promoter deletions (in 12hr-DiZ0-r1, 24hr-D0Z2-r1, and 12hr-DiZ2-r1) in the alignments to the wild-type reference, based on coverage profiles and anomalous mate pairs. Still, the reads aligned without major problems to reference genomes with the deletions included (not shown), supporting the validity of the deletions. Finally, we considered the 78 bp deletion in the activator domains of rtTA (occurring in condition 24hr-D2Z0-r3, **Appendix Table S3**). The alignment to the wild-type reference near the 78 bp deletion produced a spurious point mutation (**Appendix Figure S4E**, top), which was not resolved by aligning to a reference with the deletion included (**Appendix Figure S4F**, bottom). Moreover, the new alignment produced a signature of enhanced coverage reminiscent of a duplication; this is because the 78 bp deletion eliminates two of the three activator domains, but since most of the population (~70%) does not have the deletion, their reads appear to have a duplication relative to a reference that includes the deletion.

3. Computational and mathematical models of PF circuit and evolutionary dynamics

In this section we introduce mathematical models capturing the dynamics of PF cells and the evolutionary dynamics of PF cell populations. In section 3.1, we describe a model of the dynamics of intact PF cells prior to experimental evolution. The subsequent two sections describe our two models of evolutionary dynamics. The first of these is an ordinary differential equation (ODE) model that describes how the number of cells with wild-type and various mutant genotypes vary over time, based on their fitness. The second is a more detailed model that explicitly accounts for phenotypic switching and resuspensions during our evolution experiment.

3.1. Model of PF cell dynamics and parameter estimation

We consider a model of PF cell dynamics described in previous work (Nevozhay et al, 2012). We defined the cellular fitness function $g(Z,D,F)$ that describes how the division rate of cells with gene expression (fluorescence) F depends on extracellular Zeocin (Z) and Doxycycline (D) concentrations. In the function $g(Z,D,F)$, F represents both rtTA and yEGFP::zeoR protein levels, which we assumed to be proportional (since they are expressed from identical promoters). Cellular fitness $g(Z,D,F)$ was assumed to be a product of a constant (g_0) and two functions: the Zeocin effect $\gamma_Z(Z,F)$ and the Doxycycline effect $\gamma_D(D,F)$, each obtained from simple biochemical considerations. The population fitness is obtained by averaging the cellular fitness over the gene expression distribution $p(F)$, $G(Z,D)=\left\langle g(Z,D,F)\right\rangle_F=\int_F g(Z,D,F)p(F)dF$.

First, we considered the Zeocin effect $\gamma_Z(Z,F)$ to be proportional to the amount of DNA undamaged by Zeocin binding. Damaged DNA arises from intracellular Zeocin binding to DNA, and is constantly repaired at a fast rate. Undamaged DNA thus depends inversely on the amount of intracellular Zeocin, $Z_i(Z,F)$. We model the Zeocin effect in the following way:

$$\gamma_Z(Z,F)=\frac{\chi}{Z_i\left(Z,F\right)+\chi}. \qquad (1)$$

where χ is the Zeocin-DNA association constant. Note that the intracellular Zeocin concentration Z_i is always smaller than the extracellular Zeocin concentration Z. The rate of change for intracellular Zeocin concentration Z_i depends on the balance between Zeocin gain and loss. Zeocin gain equals the influx from extracellular medium ϕZ, where ϕ is the rate of extracellular Zeocin influx. Zeocin loss equals the outflux/dilution $h_z Z_i$ (h_z is the combined outflux/dilution rate of internal Zeocin) and the flux of yEGFP::zeoR binding to Zeocin, sRZ_i (s is the rate of Zeocin binding to yEGFP::zeoR), which converts the free form of this protein, R, into the Zeocin-bound form, B. We obtain the following rate equation for intracellular Zeocin:

$$\dot{Z}_i=\phi Z-h_z Z_i-sRZ_i. \qquad (2a)$$

Likewise, the rate of concentration change for the Zeocin-bound form, B, of yEGFP::zeoR is:

$$\dot{B} = sRZ_i - gB, \tag{2b}$$

where g is the cellular growth rate that causes protein dilution.

Together with the constraint $R+B=F$ (total yEFGP::zeoR, consisting of free and unbound forms), at steady state we obtain from (2a) and (2b) the quadratic equation:

$$sh_z\hat{Z}_i^2 + (gh_z + sgF - s\phi Z)\hat{Z}_i - g\phi Z = 0 \tag{2c}$$

We solve (2c) to find the steady state of $Z_i(Z,F)$, $\hat{Z}_i$. This quasi-steady state approximation of these processes gives the Zeocin effect $\gamma_Z(Z,F)$ in the form:

$$\gamma_Z(Z,F) = \frac{\chi}{\hat{Z}_i\left(Z,F\right) + \chi}. \tag{3}$$

We estimated the value of the Zeocin-DNA association constant χ considering that the growth rate in Zeocin (D0Z2) is approximately $g_0/2$. Since $\phi Z/h_z$ is the steady-state intracellular Zeocin concentration (**Eqn. 2a**), we obtain $\chi = \phi Z/h_z$.

We next consider the effect of Doxycycline on fitness, $\gamma_D(D,F)$. We assumed that active Doxycycline-bound rtTA (denoted A) has a first-order Hill-type inhibitory contribution to the Doxycycline effect $\gamma_D(D,F)$. Similar to the Zeocin effect, we calculated $\gamma_D(D,F)$ considering that this toxic form of rtTA arises from Doxycycline binding to free rtTA:

$$\gamma_D(D,F) = \frac{\alpha}{\alpha + A} = \frac{\alpha}{\alpha + F\dfrac{D}{D+\beta}}, \tag{4}$$

where the parameter α describes the toxicity of activated rtTA, and β describes the binding efficiency of rtTA to Doxycycline.

To estimate the parameters s, ϕ, g_0, α, and β (note that h_z is not a free parameter as we estimated it *a priori*), we performed nonlinear fitting by minimizing the objective function

$$\Omega = \sum_{D,Z}\left(G_E\left(D,Z\right) - g_0\left\langle\gamma_Z\left(Z,F\right)\gamma_D\left(D,F\right)\right\rangle\right)^2, \tag{5}$$

where the sum is over the 13 Doxycycline and Zeocin concentrations (indicated by crosses below) at which we measured population fitness G_E (**Appendix Figure S1A**):

	Dox=0.0 µg/mL	Dox=0.2 µg/mL	Dox=0.5 µg/mL	Dox=1.0 µg/mL	Dox=2.0 µg/mL
Zeo=0.0 mg/mL	✖	✖	✖	✖	✖
Zeo=0.5 mg/mL	✖				
Zeo=1.0 mg/mL	✖				
Zeo=1.5 mg/mL	✖				
Zeo=2.0 mg/mL	✖	✖	✖	✖	✖

The resulting parameter values are given in **Appendix Table S1**.

Once known, we can use the cellular fitness function $g(Z,D,F)$ to predict the cellular and/or population fitness levels at arbitrary concentrations of Doxycycline and Zeocin. Since the distribution of fluorescence levels (expression) tends to be tightly concentrated around a high value, a low value, or both (bimodal), we can use the inferred cellular fitness function and the fluorescence distribution to coarse-grain the model into two effective expression states. We define high (H) and low (L) expressor populations relative to an expression threshold θ. Then the average fitness of high and low expressor cells is

$$g_H(Z,D) = \left\langle g(Z,D,F) \right\rangle_{F>\theta} = \int_{F>\theta} g(Z,D,F)\,p(F)\,dF, \tag{6a}$$

$$g_L(Z,D) = \left\langle g(Z,D,F) \right\rangle_{F<\theta} = \int_{F<\theta} g(Z,D,F)\,p(F)\,dF. \tag{6b}$$

Knowing the fitness values g_H and g_L, the switching and growth of H and L cells are described by the system of equations:

$$\begin{cases} \dfrac{dL}{dt} = g_L L + fH - rL \\ \dfrac{dH}{dt} = g_H H - fH + rL \end{cases} \tag{7a}$$

where r is the "rise" rate of switching from low to high expression, and f is the "fall" rate of switching from high to low expression. From these equations we can calculate the values of the population growth rate g_T, and the ratio of H and L cell fractions R_∞ after the initial transient period has passed:

$$g_T = \frac{g_L - r + g_H - f + \sqrt{(g_H - f - g_L + r)^2 + 4rf}}{2} \quad (7b)$$

$$R_\infty = \frac{L}{H} = \frac{2f}{h - l + \gamma} = \frac{l - h + \gamma}{2r} = \frac{2f}{g_H - f - g_L + r + \sqrt{(g_H - f - g_L + r)^2 + 4rf}} \quad (7c)$$

Since we can determine R_∞ after directly measuring the number of H and L cells (by flow cytometry and cell counting), as well as the overall population growth rate g_T, these equations uniquely define the unknown switching rates *f* and *r*.

This is how we obtained the "ancestral" values of g_H, g_L, *f*, and *r* for each environmental condition. These values are listed in **Appendix Table S1**. We assumed that Zeocin did not affect the switching rates *f* and *r*.

3.2. Mathematical model of evolutionary dynamics

We now consider a simple deterministic model of how PF cells grow and mutate as a population of haploid asexual cells that are initially clonal (genetically identical). We assume that potentially beneficial mutations enter this ancestral population at a constant overall rate μ, measured per genome per generation. Each incoming mutation is grouped into one of a discrete number of classes denoted *i*, corresponding to mutant populations of size M_i. Each class is characterized by its fitness, f_i. The ancestral genotype's population size is M_0 and its fitness is f_0. The probability of an incoming mutation (on the ancestral genotype background) belonging to class $i \neq 0$ is P_i. We assume that the total population size $N = \sum_i M_i$ remains constant in time.

Our goal is to develop a system of ordinary differential equations (ODEs) that describes the population size of each genotype *i* over time. This requires knowing the "gain" and "loss" rates of each genotype as a function of all genotypes present in the population. Therefore, we defined the influx (gain) and outflux (loss) rates for each genotype as follows.

To obtain the influx rate of new genotypes arising from mutations on the ancestral genotype background we assumed that mutations arise strictly due to errors during the genome replication phase of the cell cycle. Therefore, the number of potentially beneficial mutations arising per unit time should be proportional to the number of genome replications (which is equal to the number of cell divisions) per unit time. For simplicity we ignored the possibility of multiple mutations co-occurring in the same genome. To estimate how many cell divisions occur per unit time, we considered the exponential growth law, according to which the rate of new cell birth in a sufficiently short time interval Δt is proportional to the current number of ancestral genotype cells M_0 and their division rate (fitness) f_0:

$$\frac{\Delta M_0}{\Delta t} = f_0 M_0 . \quad (8)$$

Since each of these newborn cells results from a cell division (and requires a genome replication), the rate of genome replications for ancestral genotype cells is also

$$r_0 = f_0 M_0 . \tag{9}$$

If the beneficial mutation rate per genome per generation is μ then the influx of potentially beneficial mutations will be

$$\Phi_0 = \mu f_0 M_0 . \tag{10}$$

Tying mutations to cell division (or DNA replication) events is a biologically reasonable assumption because spontaneous mutations tend to arise through DNA replication errors. This does not capture the effects of irradiation or other DNA damaging agents, which can generate mutations even without replication. Zeocin is in fact a DNA-damaging agent, but the DNA damage it induces stalls replication forks until the damage is repaired – with or without leftover errors. Therefore, we can still consider only mutations tied to DNA replication for sake of simplicity and to keep our assumptions minimal.

The influx term Φ_0 in **Eqn. 10** only accounts for new potentially beneficial genotypes entering the population (a random cell acquiring a mutation). Even though a mutation appears in the population, it can still be lost by genetic drift, especially in small populations (since genetic drift forces are ~1/*N*, where N is the population size). The chance for a given mutation type $i \neq 0$ to survive drift or "establish" is typically given as $p_i(Est) = 2s_i$, in terms of the selection coefficient (Kimura, 1964)

$$s_i = \frac{f_i - F}{F}, \tag{11}$$

where $F = \dfrac{\sum_j f_j M_j}{\sum_j M_j}$ is the average fitness over all genotypes.

We considered the influx of new genotypes that survive drift, while ignoring all other mutations because they go extinct very rapidly. Hence, the effective influx of genotypes M_i that carry a potentially beneficial mutation of type *i* and survive drift equals:

$$\Phi_0 \times P_i \times p_i(Est) = 2\mu f_0 M_0 P_i \frac{f_i - F}{F}, \tag{12}$$

where P_i, the probability of the incoming mutation to be of type *i*, obeys $\sum_{i \neq 0} P_i = 1.$

Assuming exponential growth for each sub-population genotype and enforcing constant total population size, we obtain a system of ODEs that describes the evolutionary dynamics:

$$\frac{dM_i}{dt} = 2\mu f_0 M_0 P_i \frac{f_i - F}{F} + f_i M_i - F M_i, \qquad \text{for } i \neq 0$$

$$\frac{dM_0}{dt} = -\frac{2\mu f_0 M_0}{F}\sum_{i>0} P_i(f_i - F) + f_0 M_0 - F M_0 \tag{13}$$

We now apply this model specifically to PF cells. Let the three mutant types be *K*, *T*, *G* with fitnesses f_K, f_T, f_G assigned as follows (using parameters from **Appendix Table S1)**:

f_K = ancestral genotype population fitness in D0Zx, where Zx indicates the current Zeocin concentration;

f_T = a uniformly distributed number ranging between $[0, f_K]$;

f_G = 0 in DxZ0; otherwise a uniformly distributed value from $[0, f^*]$ where f^* = height of the cellular fitness peak. For each condition, there is a single fitness maximum (see **Fig. 1B**). We chose values from the uniform distribution because it is the most unbiased assumption (any other distribution would imply that certain fitness values are more likely to occur than others).

The system of ODEs for the PF cells is therefore:

$$\frac{dM_K}{dt} = 2\mu f_0 M_0 P_K \frac{f_K(M_0 + M_T + M_G) - (f_0 M_0 + f_T M_T + f_G M_G)}{f_0 M_0 + f_K M_K + f_T M_T + f_G M_G} + f_K M_K - M_K \frac{f_0 M_0 + f_K M_K + f_T M_T + f_G M_G}{M_0 + M_K + M_T + M_G} \tag{14a}$$

$$\frac{dM_T}{dt} = 2\mu f_0 M_0 P_T \frac{f_T(M_0 + M_K + M_G) - (f_0 M_0 + f_K M_K + f_G M_G)}{f_0 M_0 + f_K M_K + f_T M_T + f_G M_G} + f_T M_T - M_T \frac{f_0 M_0 + f_K M_K + f_T M_T + f_G M_G}{M_0 + M_K + M_T + M_G} \tag{14b}$$

$$\frac{dM_G}{dt} = 2\mu f_0 M_0 P_G \frac{f_G(M_0 + M_K + M_T) - (f_0 M_0 + f_K M_K + f_T M_T)}{f_0 M_0 + f_K M_K + f_T M_T + f_G M_G} + f_G M_G - M_G \frac{f_0 M_0 + f_K M_K + f_T M_T + f_G M_G}{M_0 + M_K + M_T + M_G} \tag{14c}$$

$$\frac{dM_0}{dt} = -2\mu f_0 M_0 \frac{(f_K P_K + f_T P_T + f_G P_G) M_0 - f_0 (P_K + P_T + P_G) M_0}{f_0 M_0 + f_K M_K + f_T M_T + f_G M_G} - 2\mu f_0 M_0 \frac{(f_T - f_K)(P_T M_K - P_K M_T) + (f_G - f_K)(P_G M_K - P_K M_G) + (f_G - f_T)(P_G M_T - P_T M_G)}{f_0 M_0 + f_K M_K + f_T M_T + f_G M_G} + f_0 M_0 - M_0 \frac{f_0 M_0 + f_K M_K + f_T M_T + f_G M_G}{M_0 + M_K + M_T + M_G} \tag{14d}$$

We solve this ODE system numerically, scanning the mutation rate μ and the mutation type probabilities P_K and P_T to predict the population structure [M_0, M_K, M_T, M_G] and half-life of the ancestral genotype in **Appendix Figure S2**.

3.3. Evolutionary simulation framework

We developed a more detailed simulation method to predict the population dynamics of mutations arising randomly in periodically resuspended, liquid cell cultures. The framework is a hybrid between the deterministic population dynamics model presented in **Eqn. 7a** above, which captured switching rates between high and low PF gene circuit expressors as well as their condition-dependent growth rates, and a Poisson process producing mutant alleles from the ancestral genotype population (**Appendix Figure S1C**). The purpose of this framework is to predict the range of possible evolutionary dynamics by representing what we believe to be the most important factors dictating the initial evolutionary dynamics of PF-carrying populations in conditions with or without inducer (Doxycycline) and antibiotic stress (Zeocin). Most parameters used in the framework were estimated from our characterization of the fitness landscape (**Fig. 1B**) or in previous work (Nevozhay et al, 2012). Overall, we were left with four free parameters that are scanned as outlined below: beneficial mutation rates with and without Zeocin (μ_{+Z}; μ_{-Z}), and probabilities of the types of mutations that can arise as outlined in the main text. Finally, using the scans we were able to select values for the free parameters that offer excellent agreement with our evolution experiments.

We approximate each yeast cell carrying the PF synthetic gene circuit by a two-state model of growth and phenotypic switching as described above (**Eqn. 7**). Therefore, the mean time (in generations) a cell remains in a given expression state is τ_L=ln(2)/r for L cells and τ_H=ln(2)/f for H cells, which we can interpret as the "memory" of that state. We assumed that the switching rates r and f depend on the Doxycycline concentration, while the growth rates g_H and g_L depend on the concentrations of both Doxycycline and Zeocin. Next, we outline the evolutionary simulation algorithm (implemented in Python 3.4), followed by a description of each step in the algorithm.

We begin each simulation with a single population of 10^6 cells all with the ancestral genotype and in the L expression state, similar to the experiments. All parameters g_L, g_H, r, and f for the ancestral genotype (**Appendix Table S1**) are obtained by fitting as described above, using experimental fitness and gene expression measurements in 13 different Doxycycline and Zeocin concentrations (**Fig. 1B, Appendix Figure S1A**).

To simulate potentially beneficial mutant alleles as they arise, we randomly generated and introduced them into the population as a Poisson process with an overall rate of μ (/genome /generation). Each simulated mutant is described by the parameter set [g_{Lp}, g_{Hp}, r_p, f_p], where the subscript "p" (for "perturbation") indicates that the parameter might differ from its ancestral value. Mutants can be classified into one of three types based on their parameter set. The three mutation classes are:

1. K type or "Knockout" mutations: [g_{Lp}, g_{Hp}, r_p, f_p]=[g_L, g_L, 0, g_H]. They correspond to complete knockout of rtTA function. We assumed both H and L cells of K mutants to grow at rate g_L.
2. T type or "Tweaking" mutations: [g_{Lp}, g_{Hp}, r_p, f_p]=[g_L, g_{Hp}, $r_p(g_{Hp})$, $f_p(g_{Hp})$]. These mutations affect the induction dynamics of the PF gene circuit without destroying it, jointly altering the parameters g_H, r, and f. Considering that rtTA mutations affect both the growth rate and stability of the H expression state, a random change from g_H to g_{Hp} should impose associated changes from r to r_p and from f to f_p. Therefore, we modeled the relationship between τ_{Lp}, τ_{Hp} and g_{Hp} assuming that all of these variables depend on the Doxycycline concentration D.

For simplicity, we postulated that g_{Hp} and the Doxycycline concentration D are linearly related: $D = a\, g_{Hp} + b$, which is equivalent to $g_{Hp} = (D - b)/a$. There are two free parameters in this relationship. We can determine them on the grounds that the relationship must satisfy two constraints. First, at the maximum concentration D_{max} (e.g., if cells evolve in D2Z0, D_{max} = [Dox] = 2 μg/ml), we should have $g_{Hp} = g_H$ (ancestral growth rate). Second, the maximum possible growth rate should be attained at minimum effective amount of Doxycycline to which the circuit is sensitive, D_{min}, defined by $D_{min} = D_{max}(1 - g_{Hmax}/g_0)$: $g_{Hmax} = g_{Hp}(D_{min})$. Solving these two equations allows us to obtain a and b in terms of D_{min}, D_{max}, g_H, and g_{Hmax}. Thus we obtain the slope a=-(D_{max}-D_{min})/(g_{Hmax}-g_H) and the intercept $b = D_{max} - ag_H$. In expanded form the linear mapping between g_{Hp} and D is:

$$D = \frac{D_{max} - D_{min}}{g_{Hmax} - g_H}(g_H - g_{Hp}) + D_{max} \tag{15}$$

The value D also defines the half-lives $\tau_L = log(2)/r$ and $\tau_H = log(2)/f$ of the L and H states. We applied a phenomenological model to interpolate the relationship between τ_{Lp} and τ_{Hp} and inducer concentration D extracted from experimental data (**Fig. 1**; **Appendix Figure S3E**):

$$\begin{aligned} \tau_{Hp} &= a_0 D + a_1 D^2 \\ \tau_{Lp} &= a_2 D^{-1} + a_3 \end{aligned} \tag{16}$$

where a_0, a_1, a_2, and a_3 are constants obtained from fitting **Eqn. 16** to the experimental data. Finally, we end up with perturbed parameters $r_p = \log(2)\Big/\left(a_2 D^{-1} + a_3\right)$ and $f_p = \log(2)\Big/\left(a_0 D + a_1 D^2\right)$.

In summary, these constraints ensure that a change from g_H to g_{Hp} also lowers the mean expression level by altering switching rates (since all are rtTA-mediated). The relevant parameter values are given in **Appendix Table S1**.

3. G type or "Generic" mutations: [g_{Lp}, g_{Hp}, r_p, f_p]=[g_{Lp}, g_{Hp}, r, f]. These are extra-rtTA mutations affecting g_L and g_H, slightly improving drug resistance independently of rtTA. We scale the fitness improvements of g_{Lp} and g_{Hp} such that they have the same percent improvement toward g_0, lower in absolute terms for g_H. Specifically, for growth rate change from g_L to g_{Lp}, we have:

   $g_{Hp} = g_H\,(g_{Lp}/g_L)\,(g_0 - g_H)/g_0$.

   Here, the factor g_{Lp}/g_L scales g_H by the level of fitness increase affecting L cells. If the fitness of H cells would increase proportionally, it would equal $g'_{Hp} = g_H\left(g_{Lp}/g_L\right)$. The factor $(g_0 - g_H)/g_0 < 1$ then lowers g'_{Hp}, in a manner proportional to how far g_H is from the fitness peak g_0.

Additionally, the three probabilities required for implementing the occurrence of mutations in these simulations are: μ, which defines the rate of potentially beneficial mutations, and two out of P(T), P(K), and P(G), which define the likelihood of each mutation type. In conditions lacking Doxycycline, the population is unimodal ($r = 0$), thus the only beneficial mutation type is G.

To determine fixation probabilities for new alleles, we need to account for two effects: the probability of extinction of slightly favorable alleles by drift, and the probability of allele loss during resuspension.

The probability of a slightly favorable mutation fixing is approximately 2*s*, where *s* is the selection coefficient of the mutant strain (Kimura, 1964). The chance of surviving resuspensions (periodic bottlenecks) has been treated before (Wahl & Gerrish, 2001). Using this earlier model with our experimental populations and resuspension frequency, we found that the chance of losing newly generated beneficial alleles is switch-like, with virtually no chance of losing a new allele by resuspensions if it arose in the first four hours after the previous resuspension, and with a very high probability of losing it thereafter. Our simulation framework used these two factors to determine the chance of a newly generated allele *i* surviving at a time *t* hours post-resuspension: $p_i(t) = 2s\theta(4-t)$ where θ is the Heaviside step function.

Considering that the total number of cells is a continuous variable in these simulations, we set the initial number of mutant cells to represent 1 in the culture assuming a population size determined by 12 hour resuspensions (cultures starting with ~10^6 cells). Mutant genotypes arising in a given simulation run all derive from the ancestral genome. For simplicity, we do not allow multiple mutations to occur in the same genome.

In the beginning of the simulations, when cells are first exposed to the environment in which they evolve, they undergo transient dynamics as Doxycycline and Zeocin diffuse into the cells and induce the PF gene circuit. We capture the transient effects of Doxycycline by the dynamics of the built-in two-state model (all cells starting as *L*, and then some switching to *H*). To capture the known delay arising as Zeocin crosses the cell and nuclear membranes and binds to DNA before affecting fitness, we use the internalization dynamics model from **Eqn. 2**, and re-estimate Zeocin internalization parameters based on our experimentally observed initial fitness dynamics in D0Z2, as detailed below. Using this algorithm, we predict dynamics of overall population fitness, populations of mutant strains, distributions of mutation classes, and timing of mutations (**Figs. 2;3F-G;4C;5F-G; Appendix Figure S2**).

3.4. Steps in the algorithm

1. **Initialization**. Assume 10^6 cells (all in state L, corresponding to the condition D0Z0). Select parameter set appropriate for environment. For Zeocin-containing environments, use a time-dependent growth rate parameter $g_L = g_0\,\gamma_Z(t)$ where g_0 is the initial fitness (in D0Z0) and $\gamma_Z(t)$ is the time-dependent fitness effect of Zeocin (Nevozhay et al, 2012). This captures the dynamics of growth rate relaxation to a lower steady state value as Zeocin, Z_i, enters the cells. This corresponds to the solution of **Eqn. 2a** above, assuming no PF circuit activity initially ($R = 0$):

$$\gamma_Z(t) = \frac{\chi}{Z_i(t) + \chi}$$
$$Z_i(t) = \frac{Z\phi}{h_z}\left(1 - e^{-h_z t}\right) \qquad (17)$$

2. **Calculate time-dependent ancestral genotype PF population size**. The total number of PF cells with intact (ancestral) genotype is: $N_{tot,PF}(t) = N_L(t) + N_H(t)$. More explicitly, with $N_H(0) = 0$ we have the time-dependent solution of **Eqn. 7a** above:

$$N_{tot}(t) = \frac{1}{2\lambda} N_L(0) e^{\omega t}\left(g_H - f - r - g_L + \lambda + e^{\lambda t}\left(f - g_H + r + g_L + \lambda\right)\right)$$
$$\omega = -\frac{1}{2}\left(f - g_H + r - g_L + \lambda\right) \qquad (18)$$
$$\lambda = \sqrt{f^2 + \left(g_H + r - g_L\right)^2 + 2f\left(r - g_H + g_L\right)}$$

3. **Generate next mutation time**. For $t \in [0, 480]$ hours, calculate the next mutation time using the effective beneficial mutation rate, μ. For a Poisson process with mutation i at time t_i, the next mutation i+1 occurs at time t_{i+1} at instantaneous rate $\frac{\mu w \mathrm{N}_{\mathrm{tot,PF}}(t_i)}{\log(2)}$, where w is the overall population fitness at time t_i and the factor w/log(2) converts the units of μ from 1/generations to 1/hours. This model is approximately correct as long as the mutation rate is sufficiently high, because then the time between mutations is short enough that the population is approximately constant between mutation events. We thus draw the mutation time t_{i+1} from the probability distribution $\mathrm{P}(t_{i+1}) = \frac{\mu w \mathrm{N}_{\mathrm{tot,PF}}(t_i)}{\log(2)} e^{-\frac{\mu w \mathrm{N}_{\mathrm{tot,PF}}(t_i)}{\log(2)} t_{i+1}}$.

   The mutation is retained in the population only if it occurs within the first four hours after a multiple of the resuspension time (12 hours) as explained in the previous section.
4. **Select the mutation type**. Let $\xi(a,b)$ be a uniformly distributed random real number in the range $[a,b]$. Each mutation event is randomly assigned to one of three classes T, K, or G with probability P(T), P(K), and P(G), respectively, implementing the perturbations depicted in **Appendix Figure S1B** (see section 3.3 above):

   •"Tweak" T

   $$g_{Hp} = \xi(g_H, g_{Hmax});\ r_p = \log(2) \Big/ \left(a_2 D^{-1} + a_3\right);\ f_p = \log(2) \Big/ \left(a_0 D + a_1 D^2\right) \tag{19a}$$

   •"Knockout" K

   $$r_p = 0;\ f_P = g_H;\ g_{Hp} = g_L \tag{19b}$$

   •"Generic" G

   $$g_{Lp} = g_L\,[1 + \xi(0, \varphi)];\ g_{Hp} = g_H\,(g_{Lp}/g_L)\,(g_0 - g_H)/g_0 \tag{19c}$$

   where φ reflects the height of the fitness peak relative to the current population fitness (roughly, the slope of the fitness landscape) in each condition. The value of φ gives the maximal attainable fitness by a G-type mutation. Its value is not critical as long as it does not allow mutations with unrealistically exaggerated benefits, while at the same time ensuring the maximal benefit without Zeocin is small. We therefore chose $\varphi = 0.8$ in Zeocin-containing conditions and $\varphi = 0.01$ in Zeocin-free conditions.
5. **Define the initial size and state of each mutant population**. When a new mutant arises after the first resuspension, we need to scale its initial population to reflect what its population would be in culture assuming that new mutants start as a single cell. We call this population M_{ic}. Numerically, we allow the population to continue growing at exponential phase for the 20 simulated days, without directly implementing resuspensions in the growing population. Therefore, the fraction of the population representing one cell increases depending on how many 12-hour blocks of time have passed. With 12-hour resuspensions: $M_{ic}(t_m) = \frac{1}{N_{tot}(0)} \sum_{i \in A} N_{tot,i}\left(12 \left\lfloor t_m / 12 \right\rfloor\right)$ where $\lfloor \circ \rfloor$ denotes the floor function, A_i is the quantity of allele i in the population, and $N_{tot}(t)$ reflects total population at time t. Each initial mutant cell is randomly selected to be in the L or H state with probability weighted by fraction of H or L cells in the intact PF population. Note that we still account for population size effects from resuspension bottlenecks, as described in Section 3.3.
6. **Continue the simulation**. Repeat steps 1 – 5 until the end time is reached.
7. **Generate dynamics**. Iterate through the 20 day simulation time in uniform steps, computing allele frequencies for the population.

3.5. Justification of parameter choices

To obtain a realistic value for the effective beneficial mutation rate μ, we need to consider the set of all deletions, base-pair substitutions, frameshifts, etc. that could possibly improve growth rates for each of the conditions where PF cells evolved. This is difficult to estimate, but an upper limit is given by the total mutation rate estimate of 3.80×10^{-10} – 6.44×10^{-10} /bp /generation (Lang & Murray, 2008). Considering the yeast genome size of approximately 10^7 bp, the beneficial mutation rate is probably a few orders of magnitude less than the overall mutation rate of 10^{-3} /genome /generation. Recently the rate of beneficial mutation was experimentally estimated at approximately 10^{-6} /genome /generation (Levy et al, 2015).

For a randomly placed beneficial mutation, what would be realistic choices for P(T), P(K), or P(G)? Because P(T) + P(K) + P(G) = 1, we only need to have estimates for two of the probabilities. On the one hand, the overall chance of extracircuit beneficial mutation may be much higher than intracircuit because of the relative quantities of genetic material. However, considering that the PF gene circuit strongly affects fitness in most environments where the cells evolve, beneficial intracircuit mutations may be more likely to establish than extracircuit mutations in the early phase of evolution. Therefore, we scanned these probabilities over 3 orders of magnitude in the simulations.

4. Extended results of evolutionary dynamics simulations

4.1. The effects of various parameters on evolutionary dynamics

To study the effects of various mutational regimes on the first adaptive step in evolution, we defined two quantitative, experimentally meaningful, measures. First, we calculated the number of mutant alleles reaching a frequency > 5% (our threshold for detection with whole-genome Illumina sequencing). Second, we determined the ancestral strain's half-life over 20 days of simulated time for a range of effective beneficial mutation rates less than 10^{-5} /genome /generation, simultaneously scanning the probabilities P(T) and P(G) (**Appendix Figure S3**).

In the condition with the least selective pressure, DiZ0, none of the mutants reached a very high frequency by Day 20. Therefore, the simulations predicted uniformly long ancestral half-life, regardless of the overall beneficial mutation rate (**Appendix Figure S3A,B**).

With higher Doxycycline (D2Z0), more mutant alleles could establish to levels >5% in 20 days, and the average ancestral genome half-life (the time for the ancestral genome frequency to reach 50% of the population) was the shortest among all conditions (**Appendix Figure S3A,B**). The beneficial mutation rate μ affects the stability of the ancestral strain (i.e. its genome half-life) most strongly at very low values of μ, where the ancestral genotype's half-life falls from nearly the maximum measurable (20 days) to around 5 days (**Appendix Figure S3B**) in the same parameter regime where the number of alleles is low. This indicates that having one or just a few mutants that improve fitness is sufficient for a fast sweep in this condition. At the same time, for $\mu > 10^{-6.5}$/genome /generation, the ancestral genotype half-life decreases less dramatically with the mutation rate (**Appendix Figure S3B**). In this regime many mutations establish, each with higher fitness than the ancestral genotype. The non-monotonic relationship between number of alleles and mutation rate in this condition reflects a large number of alleles establishing at levels below 5 percent taking up part of the population at higher mutation rates.

When both Doxycycline and Zeocin are present (DiZ2 and D2Z2), increasing μ results in a higher number of established mutants (**Appendix Figure S3A**). The number of mutants increases with P(T), while the half-life of the ancestral genotype decreases with P(T) (**Appendix Figure S3B**). The stronger

selective pressure in D2Z2 results in shorter ancestral genotype half-life than DiZ2 for most parameter values.

The effect of P(G) on the number of mutants and ancestral half-life is small for much of the parameter space (different line thicknesses reflect P(G) = 5%, 75%, and 95% for a given P(T) in **Appendix Figure S3A,B**). One exception to this is trend is D0Z2, for which the ancestral genome's half-life decreases, and the mutant allele count somewhat increases, with P(G) (**Appendix Figure S3A,B**).

Based on the relative number of total intra- and extra-circuit mutations observed in the experiments with Zeocin and simulation results reflecting them (**Fig. 2; Appendix Figure S3**) we set P(G) = 0.75 (i.e. 75 %). Probabilities P(T) and P(K) were then estimated by matching the timing and total number of emergent mutations to experimental values; see the main text. Based on that analysis, we chose the values $P(T|\neg G) = P^*(T) = 10\%$ and $P(K|\neg G) = P^*(K) = 90\%$, respectively (out of total PF-only mutations). This translated into probability values of P(T) = 2.5% and P(K) = 22.5%, the rest being generic (G-type) mutations.

4.2. Agreement between predicted and observed evolutionary dynamics

We used our calibrated simulation framework to explore the evolutionary dynamics in representative cases (**Figs. 3F,G;4C;5F,G; Appendix Figure S3D,E**). In each simulated case, the fitness transiently drops to a level dependent on the environment (i.e. quantity of Doxycycline and absence or presence of Zeocin). Then the population begins to recover at a rate proportional to the probability and benefit of mutations in that condition (**Appendix Figure S3D**). In D2Z0, fitness drops in individual simulations for the first few days, and then recovers coincidently with K alleles sweeping the population (compare **Appendix Figure S3D** and **Fig. 3F**). In DiZ0 fitness drops slightly and then recovers minimally because selection is too weak (compare **Appendix Figure S3D** and **Fig. 3G**). In D2Z2 and DiZ2 fitness drops similarly and then recovers coincidently with the rise of fitter mutant alleles (compare **Appendix Figure S3D** and **Figs. 5F,G**).

We next reconstructed time courses of mean PF gene expression (corresponding to both rtTA and ZeoR::yEGFP concentration) for the evolving, genotypically mixed population. We used cellular fitness landscapes to infer expression levels (see above). Mean expression levels initially increase, then decrease, in each condition (**Appendix Figure S3F**), except for D0Z2 and D0Z0. K mutations disable PF, causing a clear rise and then fast fall of gene expression in D2Z0 (dark blue line, **Appendix Figure S3F**). In DiZ0 gene expression drops only slightly, reflecting low selection (light blue line, **Appendix Figure S3F**). The reconstructed expression levels in DiZ2 and D2Z2 also capture the experimentally measured trends (green and magenta lines, **Appendix Figure S3F**).

5. Appendix References

DePristo MA, Banks E, Poplin R, Garimella KV, Maguire JR, Hartl C, Philippakis AA, del Angel G, Rivas MA, Hanna M, McKenna A, Fennell TJ, Kernytsky AM, Sivachenko AY, Cibulskis K, Gabriel SB, Altshuler D, Daly MJ (2011) A framework for variation discovery and genotyping using next-generation DNA sequencing data. *Nat Genet* **43:** 491-498

Garrison E, Marth G (2012) Haplotype-based variant detection from short-read sequencing. *arXiv* **q-bio.GN:** 1207.3907

Kimura M (1964) Diffusion models in population genetics. *J Appl Prob* **1:** 177-232

Lang GI, Murray AW (2008) Estimating the per-base-pair mutation rate in the yeast Saccharomyces cerevisiae. *Genetics* **178:** 67-82

Langmead B, Salzberg SL (2012) Fast gapped-read alignment with Bowtie 2. *Nat Methods* **9:** 357-U354

Levy SF, Blundell JR, Venkataram S, Petrov DA, Fisher DS, Sherlock G (2015) Quantitative evolutionary dynamics using high-resolution lineage tracking. *Nature* **519:** 181-186

Li H (2013) Aligning sequence reads, clone sequences, and assembly contigs with BWA-MEM. *arXiv* **q-bio.GN:** 1303.3997v1302

Li H, Handsaker B, Wysoker A, Fennell T, Ruan J, Homer N, Marth G, Abecasis G, Durbin R, Proc GPD (2009) The Sequence Alignment/Map format and SAMtools. *Bioinformatics* **25:** 2078-2079

McKenna A, Hanna M, Banks E, Sivachenko A, Cibulskis K, Kernytsky A, Garimella K, Altshuler D, Gabriel S, Daly M, DePristo MA (2010) The Genome Analysis Toolkit: A MapReduce framework for analyzing next-generation DNA sequencing data. *Genome Res* **20:** 1297-1303

Robinson JT, Thorvaldsdottir H, Winckler W, Guttman M, Lander ES, Getz G, Mesirov JP (2011) Integrative genomics viewer. *Nat Biotechnol* **29:** 24-26

Thorvaldsdottir H, Robinson JT, Mesirov JP (2013) Integrative Genomics Viewer (IGV): high-performance genomics data visualization and exploration. *Brief Bioinform* **14:** 178-192

Wahl LM, Gerrish PJ (2001) The probability that beneficial mutations are lost in populations with periodic bottlenecks. *Evolution* **55:** 2606-2610

6. Appendix Figure Legends

Appendix Figure S1. Fitness landscape and predicted mutations. (A) The population fitness landscape in **Fig. 1B** was fit to experimental data points in various combinations of Doxycycline and Zeocin doses. There are N = 3 replicates per environmental condition in the fitness landscape. (B) Expected mutation types that could arise in the landscape and their effects on population dynamics: ancestral genotype (PF), knockout mutations (K), tweaking mutations (T), and extra-rtTA mutations (G). Red arrows denote processes altered by each mutation type. (C) Simplified flowchart for the simulation framework provides an overview of the steps involved in predicting evolutionary dynamics.

Appendix Figure S2. Predicted environment-dependent characteristics of evolutionary dynamics. Shown are the fraction of genotypes at 20 days and half-life of ancestral genotype from the ODE model as a function of all free parameters.

(A) Calculated (predicted) fraction of wild-type (W), and K, T, and G type mutants at day 20 in DiZ0.

(B) Calculated (predicted) half-life of the ancestral genotype in DiZ0.

(C) Calculated (predicted) fraction of wild-type (W), and K, T, and G type mutants at day 20 in D2Z0.

(D) Calculated (predicted) half-life of the ancestral genotype in D2Z0.

(E) Calculated (predicted) fraction of wild-type (W), and K, T, and G type mutants at day 20 in D0Z2.

(F) Calculated (predicted) half-life of the ancestral genotype in D0Z2.

(G) Calculated (predicted) fraction of wild-type (W), and K, T, and G type mutants at day 20 in D2Z2.

(H) Calculated (predicted) half-life of the ancestral genotype in D2Z2.

(I) Calculated (predicted) fraction of wild-type (W), and K, T, and G type mutants at day 20 in DiZ2.

(J) Calculated (predicted) half-life of the ancestral genotype in DiZ2.

Appendix Figure S3. Predicted evolutionary dynamics from the simulation framework.

(A, B) Predicted effects of mutation rates on characteristics of evolutionary dynamics (number of alleles >5% of the population and half-life of the ancestral genome) in each environmental condition from **Fig. 1B**; see the legend in panel D for colors in all panels. Multiple lines of the same color but different thickness depict a scan of extra-rtTA (type G) mutation probabilities: $P(G)$=5% (thin), $P(G)$=75% (medium), and $P(G)$=95% (thick). For intra-rtTA mutations, we give the probabilities P(T) and P(K) as fractions of total intra-rtTA mutations: P*(T) = $P(T|\neg G)$ = P(T) / (1 - P(G)) and P*(K) = $P(K|\neg G)$ = P(K) / (1 - P(G)). This way we can consider the relative frequencies of intra-rtTA mutations independently of the probability of G mutations. We ran 20 simulations while scanning the effective beneficial mutation rate, μ. Error bars report mean ± SEM.

(C) Fraction of G type mutants established in DiZ2 versus $P(T)$ and $P(G)$, with $\mu_{+Z} = 10^{-5.4}$. For these parameter scans, we ran 50 simulations per point in parameter space.

(D) Sample fitness timecourses for each of the conditions, corresponding to the simulated allele frequency graphs shown in **Figs. 3-5**. For these results we ran 500 simulations per condition.

(E) Half-lives of low (τ_L) and high (τ_H) expression states of PF cells versus Doxycycline doses, estimated from experimental data. Lines represent phenomenological models given in **Eqn. 16**.

(F) Predicted fluorescence levels back-calculated from fitness landscapes (**Fig. 1B**). To calculate the fluorescence for each condition, we used the cellular fitness of high and low expressors to infer their subpopulation sizes and then estimated the mixed population-average fluorescence as a weighted mean over the subpopulations for each environment at each time point.

Appendix Figure S4. Time courses and phenotypes for evolution in D2Z0.

(A) Experimentally measured fluorescence and fitness (3 replicates) for 24 h resuspensions of PF cells in D2Z0.

(B) Allele frequency time courses from a 24 h resuspension experiment (replicate #1) in Doxycycline alone (D2Z0).

(C) Gene expression shift of clonal isolate #1 compared to the PF ancestor in condition D2Z0, 24-hour resuspensions. Clone #1 is unresponsive to inducer. All other 5 clones tested behave identically.

(D) Coverage profile of reads aligned to the wild-type reference genome (top) and a reference with the 30-bp duplication included (bottom) for a frozen sample taken at Day 19 from 12hr-D2Z0-r1. Horizontal darker bar covers original 30 bp region on top and the new 60 bp region on the bottom.

(E) Coverage profile of reads aligned to the wild-type reference genome (top) and a reference with the 78-bp deletion included (bottom) for a frozen sample taken at Day 19 from 24hr-D2Z0-r3. Horizontal darker bar covers the original 78 bp region on top, which is deleted on the bottom.

Appendix Figure S5. Time courses and phenotypes for evolution in D0Z2.

(A) Experimentally measured fluorescence and fitness (3 replicates) for 24 h resuspensions of PF cells in D0Z2.

(B) Time course of allele frequencies inferred directly from whole-genome sequencing of frozen samples in D0Z2 experiment with 24 h resuspensions, replicate #1. Sanger sequencing showed linkage between some alleles that whole-genome sequencing could not detect (**Fig. 4B**).

(C) Two control strains (PX and NR) and their basal expression levels compared to PF cells. PX lacks yEGFP:ZeoR, while NR is a different gene circuit with higher basal expression of yEGFP:ZeoR.

(D) Fitness of PX versus PF cells in D0Z2 over several days. Cells without yEGFP:ZeoR vanish after 1 day in D0Z2.

(E) Growth curve of NR versus PF cells in various Zeocin concentrations. NR resists Zeocin better due to its higher basal expression.

Appendix Figure S6. Time courses and phenotypes for evolution in D2Z2.

(A) Experimentally measured fluorescence and fitness (3 replicates) for 24 h resuspensions of PF cells with 24 h resuspensions in Doxycycline inducer and Zeocin antibiotic stress (D2Z2).

(B) Time course of allele frequencies inferred from next-generation and Sanger sequencing of frozen samples in environment D2Z2 with 24 hour resuspensions, replicate #1.

(C) Tradeoffs between fitness in the presence and absence of Zeocin for the ancestral PF gene circuit and clones evolved in D2Z2.

(D) Experimentally measured fluorescence and fitness replicates for resuspensions of PF cells in media containing neither Doxycycline inducer nor Zeocin (D0Z0) with 12-hour resuspensions.

(E) Experimentally measured fluorescence and fitness replicates for resuspensions of PF cells in media containing neither Doxycycline inducer nor Zeocin (D0Z0) with 24-hour resuspensions.

Appendix Figure S7. Phenotyping of clones and reconstructed mutants.

(A) Gene expression distributions of clonal isolate #1 from DiZ2 in various conditions.

(B) Phenotypes of mutations reconstructed in the ancestral background. Mutations are from clones #1 and #2 evolved in Doxycycline and Aeocin (D2Z2, "suboptimal response"). Top: log10-ratio of fitness with Doxycycline (D2Zy) relative to no Doxycycline (D0Zy) either with or without Zeocin (y=0 or y=2). Middle: log10-ratio of average fluorescence intensity with Doxycycline (D2Zy) relative to no Doxycycline (D0Zy). Bottom: log10-ratio of fitness with Zeocin (DxZ2) relative to no Zeocin (DxZ0), either with or without Doxycycline (x=0 or x=2). Error bars represent standard deviations around the mean. Stars denote significance at $P<0.05$.

(C) Gene expression of clonal isolate #1 and the corresponding reconstructed strain (dashed line) from D2Z2 in various conditions.

(D) Gene expression of clonal isolate #2 and the corresponding reconstructed strain (dashed line) from D2Z2 in various conditions.

Appendix Figure S8. Predicted frequencies of pre-existing mutations in the simulation framework. To simulate the effect of pre-existing neutral mutations on evolutionary dynamics, we performed a simulation with neither Doxycycline nor Zeocin (D0Z0) for 24h. We saved all of the neutral PF mutations that arose, and then simulated further evolution in one of the five Doxycycline- and/or Zeocin-containing conditions (D2Z0, DiZ0, D0Z2, D2Z2, DiZ2). (A) Final allele frequency (at Day 20) of mutants that arose neutrally in the initial 24h simulation time. Error bars represent the SEM. (B) Comparison between simulations with one day of neutral mutation accumulation (P, "preexisting") and without it (A, "purely ancestral") reveals nearly identical mean and standard deviation of the ancestral genotype's half-life in all conditions. Error bars: standard deviation. $N = 500$ runs.

7. Appendix Tables

Param	Value					Notes
μ_{+Z}	$10^{-5.4}$ /genome /generation					Mut. rate in Zeocin.
μ_{-Z}	$10^{-6.2}$ /genome /generation					Mut. rate without Zeocin.
h_z	0.1 /h					Zeocin outflux rate.
Z	2 mg/ml					Zeocin concentration.
χ	0.01076 mg/ml					$\chi = \phi Z/h_z$; Zeocin-DNA assoc.
s	186.7983 ml/(h mg)					Zeocin-ZeoR association rate.
ϕ	5.38×10^{-4} /h					Zeocin internalization rate.
α	0.2229 mg/ml					rtTA toxicity.
β	0.4424 mg/ml					Dox - rtTA association.
g_0	0.2634 /h					Ancestral growth rate in D0Z0.
g_{Li}	g_0					Initial growth rate in Zeocin.
a_0 (τ_H)	1091.07					Params. for curves in **Appendix Figure S2E**.
a_1 (τ_H)	320.901					
a_2 (τ_L)	14.1197					
a_3 (τ_L)	-1.28361					
	DiZ0	**DiZ2**	**D2Z0**	**D2Z2**	**D0Z2**	Condition-specific rates. /h
g_L	g_0	0.50 g_0	g_0	0.50 g_0	0.50 g_0	Low expressor growth rate.
g_H	0.75 g_0	0.75 g_0	0.60 g_0	0.60 g_0	N/A	High expressor growth rate.
r	0.01	0.01	0.12	0.12	0.0000	L → H switch rate.
f	0.003	0.003	0.0002	0.0002	N/A	H → L switch rate.
g_{Hmax}	g_0	g_0	g_0	0.9 g_0	g_0	Maximum possible g_H.

Appendix Table S1. Parameters used in mathematical and computational models of PF gene circuit evolution.

Experiment D0Z0	Location	Mutation	Read counts	
			Day 1	Day 19
12hr, r1	*RAD1* 1350 (chr 16: 508,046)	A → C (Synonymous)	Illumina: 9% (6/68) Sanger: NA	Illumina: 14% (5/37) Sanger: NA

Appendix Table S2. Mutations detected by whole-genome Illumina sequencing and targeted Sanger sequencing in condition D0Z0 (galactose-only). *In all subsequent mutation tables (Appendix* ***Tables S3-S5****) the first column indicates the experiment (12 hr or 24 hr resuspension, and replicate number). The second column indicates the genomic location; we list the nearest feature and the 1-based coordinate relative to that feature (i.e., coordinate 1 is the first base in the gene, while -1 is the last base before the gene, both in the frame of transcription), as well as the chromosomal coordinate (Watson strand) with respect to the S288c reference. The third column lists the effect of the mutation (base changes are with respect to the Watson strand). The remaining columns show the read counts at various days in the experiment. "NA" indicates that sequencing method was not performed at that day, while a gray box indicates neither sequencing method was performed. An asterisk indicates that the mutation did not pass filters, but we report it here for completeness.*

(A) Experiment DiZ0	Location	Mutation	Read counts		
			Day 9	Day 13	Day 19
12hr, r1	rtTA -212 (chr 15: 729,394)	42 bp deletion	Illumina: 0% Sanger: NA	Illumina: NA Sanger: 0%	Illumina: 0% Sanger: 58% (7/12)
12hr, r2	Illumina: NA Sanger: None				
12hr, r3	Illumina: NA Sanger: None				

(B) Experiment D2Z0	Location	Mutation	Read counts	
			Day 9	Day 19
12hr, r1	rtTA 123 (chr 15: 729,728)	G → T (Leu → Phe)	Illumina: 46% (45/97) Sanger: 50% (6/12)	Illumina: 1% (1/69)* Sanger: 0%
	rtTA 153 (chr 15: 729,758)	G → C (Leu → Phe)	Illumina: 11% (12/108) Sanger: 25% (3/12)	Illumina: 0% Sanger: 0%
	rtTA 196 (chr 15: 729,801)	C → G (His → Asp)	Illumina: 11% (13/121) Sanger: 8% (1/12)	Illumina: 98% (58/59) Sanger: 100% (12/12)
	rtTA 410 (chr 15: 730,015)	T → G (Val → Gly)	Illumina: 13% (15/120) Sanger: 8% (1/12)	Illumina: 0% Sanger: 0%
12hr, r2	rtTA 189 (chr 15: 729,796)	C → G (His → Gln)		Illumina: NA Sanger: 40% (4/10)
	rtTA 514 (chr 15: 730,121)	C → T (Gln → stop)		Illumina: NA Sanger: 60% (6/10)
12hr, r3	rtTA 77 (chr 15: 729,684)	C → G (Thr → Arg)		Illumina: NA Sanger: 10% (1/10)
	rtTA 129 (chr 15: 729,736)	G → C (Trp → Cys)		Illumina: NA Sanger: 30% (3/10)
	rtTA 145 (chr 15: 729,752)	C → T (Arg → Trp)		Illumina: NA Sanger: 50% (5/10)
	rtTA 577 (chr 15: 730,182)	3 bp deletion		Illumina: NA Sanger: 10% (1/10)

			Day 2	Day 5	Day 8	Day 9	Day 10	Day 19
24hr, r1	rtTA 91 (chr 15: 729,696)	G → C (Ala → Pro)	Illumina: <1% (1/146)* Sanger: NA	Illumina: 5% (6/116) Sanger: NA	Illumina: NA Sanger: 10% (1/10)	Illumina: NA Sanger: 10% (1/10)	Illumina: 4% (6/161)* Sanger: NA	Illumina: 2% (2/85)* Sanger: 0%
	rtTA 95 (chr 15: 729,700)	30 bp tandem duplication	Illumina: 0% Sanger: NA	Illumina: 0% Sanger: NA	Illumina: NA Sanger: 60% (6/10)	Illumina: NA Sanger: 10% (1/10)	Illumina: 0% Sanger: NA	Illumina: 0% Sanger: 58% (7/12)
	rtTA 454 (chr 15: 730,059)	C → T (Gln → stop)	Illumina: 0% Sanger: NA	Illumina: 0% Sanger: NA	Illumina: NA Sanger: 10% (1/10)	Illumina: NA Sanger: 0%	Illumina: <1% (1/191)* Sanger: NA	Illumina: 2% (1/57)* Sanger: 0%
	rtTA 609 (chr 15: 730,214)	T → A (Cys → stop)	Illumina: 1% (2/134)* Sanger: NA	Illumina: 52% (63/121) Sanger: NA	Illumina: NA Sanger: 20% (2/10)	Illumina: NA Sanger: 20% (2/10)	Illumina: 50% (83/167) Sanger: NA	Illumina: 40% (20/50) Sanger: 42% (5/12)
24hr, r2	rtTA 179 (chr 15: 729,784)	T → C (Leu → Ser)						Illumina: 4% (3/75)* Sanger: 10% (1/10)
	rtTA 442 (chr 15: 730,047)	G → T (Glu → stop)						Illumina: 51% (38/74) Sanger: 50% (5/10)
	rtTA 562 (chr 15: 730,167)	T → C (Phe → Leu)						Illumina: 29% (28/95) Sanger: 40% (4/10)
24hr, r3	rtTA 13 (chr 15: 729,618)	G → T (Asp → Tyr)						Illumina: 21% (15/73) Sanger: 50% (5/10)
	rtTA 275 (chr 15: 729,880)	G → A (Ser → Asn)						Illumina: 8% (5/63) Sanger: 10% (1/10)
	rtTA 346 (chr 15: 729,951)	C → A (Gln → Lys)						Illumina: 1% (1/76)* Sanger: 10% (1/10)
	rtTA 651 (chr 15: 730,256)	78 bp deletion						Illumina: 0% Sanger: 30% (3/10)

Appendix Table S3. Mutations detected by whole-genome Illumina sequencing and targeted Sanger sequencing in conditions DiZ0 and D2Z0.

(A) Mutations in condition DiZ0. All columns are as indicated for ***Appendix Table S2****.*

(B) Mutations in condition D2Z0. All columns are as indicated for ***Appendix Table S2****.*

Experiment D0Z2	Location	Mutation	Read counts			
			Day 9		Day 19	
12hr, r1	*INO2* -159 *YDR124W* -688 (chr 4: 699,627)	A → deletion	Illumina: 2% (4/176)* Sanger: NA		Illumina: 28% (21/75) Sanger: 20% (2/10)	
	YHR127W 613 (chr 8: 361,525)	G → A (Ala → Thr)	Illumina: 7% (12/178) Sanger: NA		Illumina: 8% (7/91) Sanger: 0%	
	GAL2 692 (chr 12: 290,903)	G → T (Gly → Val)	Illumina: 2% (3/190)* Sanger: NA		Illumina: 29% (26/89) Sanger: 20% (2/10)	
	GAL2 1006 (chr 12: 291,217)	T → A (Phe → Ile)	Illumina: 5% (9/191) Sanger: NA		Illumina: 14% (11/78) Sanger: 20% (2/10)	
			Day 3	Day 9	Day 14	Day 19
24hr, r1	*YDR186C* 1742 (chr 4: 833,751)	T → A (Synonymous)	Illumina: <1% (1/277)* Sanger: NA	Illumina: 6% (5/89) Sanger: 0%	Illumina: 8% (8/101) Sanger: NA	Illumina: <1% (2/313)* Sanger: 0%
	CHO2 2567 (chr 7: 805,006)	A → C (His → Pro)	Illumina: 0% Sanger: NA	Illumina: 1% (1/74)* Sanger: NA	Illumina: 5% (6/119) Sanger: NA	Illumina: 14% (45/316) Sanger: NA
	Intergenic (just after RPS0A) (chr 7: 921,790)	T → deletion	Illumina: 0% Sanger: NA	Illumina: 0% Sanger: NA	Illumina: 8% (11/134) Sanger: NA	Illumina: 12% (37/302) Sanger: 30% (3/10)
	SRX1 -93 *CYT2* -325 (NHP6A binding site) (chr 11: 278,188)	T → A	Illumina: 0% Sanger: NA	Illumina: 7% (7/100) Sanger: 0%	Illumina: 12% (11/94) Sanger: NA	Illumina: 1% (4/323)* Sanger: 0%
	SIN4 2838 *YNL235C* 213 (chr 14: 209,767)	A → deletion (frameshift)	Illumina: 3% (7/275)* Sanger: NA	Illumina: 5% (5/91) Sanger: NA	Illumina: 7% (9/125) Sanger: NA	Illumina: <1% (1/267)* Sanger: NA
	EOS1 603 (chr 14: 477,430)	A → C (Synonymous)	Illumina: 0% Sanger: NA	Illumina: 1% (1/92)* Sanger: NA	Illumina: 8% (9/117) Sanger: NA	Illumina: 11% (35/305) Sanger: 40% (4/10)
	yEFGP::zeoR -219 (chr 15: 723,701)	42 bp deletion	Illumina: 0% Sanger: NA	Illumina: 0% Sanger: 80% (8/10)	Illumina: 0% Sanger: NA	Illumina: 0% Sanger: 60% (6/10)
	GUP2 1250 (chr 16: 190,403)	A → deletion (frameshift, leads to premature stop)	Illumina: 4% (10/255)* Sanger: NA	Illumina: 11% (12/106) Sanger: 10% (1/10)	Illumina: 5% (5/96) Sanger: NA	Illumina: <1% (1/309)* Sanger: NA
24hr, r2	*yEFGP::zeoR* 831 (chr 15: 724,750)	G → A (Synonymous)				Illumina: 29% (56/194) Sanger: 70% (7/10)
24hr, r3	Illumina: None Sanger: NA					

Appendix Table S4. Mutations detected by whole-genome Illumina sequencing and targeted Sanger sequencing in conditions D0Z2 (antibiotic only).

All columns are the same as for ***Appendix Table S2****.*

(A) Experiment DiZ2	Location	Mutation	Read counts	
			Day 9	Day 19
12hr, r1	*STB3* -66 (chr 4: 793,955)	C → G	Illumina: 15% (15/97) Sanger: NA	Illumina: 17% (12/69) Sanger: 10% (1/10)
	GAL2 568 (chr 12: 290,779)	A → C (Ile → Leu)	Illumina: 27% (32/118) Sanger: NA	Illumina: 78% (63/81) Sanger: 80% (8/10)
	GAL2 1061 (chr 12: 291,272)	C → A (Thr → Asn)	Illumina: 29% (36/125) Sanger: NA	Illumina: 26% (23/88) Sanger: 20% (2/10)
	rtTA -261 (chr 15: 729,345)	42 bp deletion	Illumina: 0% Sanger: NA	Illumina: 0% Sanger: 70% (7/10)
12hr, r2	Illumina: NA Sanger: None			
12hr, r3	Illumina: NA Sanger: None			

(B) Experiment D2Z2	Location	Mutation	Read counts						
			Day 9			Day 19			
12hr, r1	rtTA -15 (chr 15: 729,591)	C → G	Illumina: 13% (36/276) Sanger: NA			Illumina: 54% (63/116) Sanger: NA			
	rtTA 225 (chr 15: 729,830)	G → C (Trp → Cys)	Illumina: 10% (25/252) Sanger: NA			Illumina: 48% (68/141) Sanger: NA			
			Day 5	Day 9	Day 10	Day 12	Day 15	Day 18	Day 19
24hr, r1	rtTA -9 (chr 15: 729,597)	G → C	Illumina: 0% Sanger: NA	Illumina: 9% (11/127) Sanger: 40% (4/10)	Illumina: 11% (15/132) Sanger: NA	Illumina: 18% (24/132) Sanger: NA	Illumina: 65% (93/142) Sanger: NA	Illumina: NA Sanger: 70% (7/10)	Illumina: 51% (53/103) Sanger: NA
	rtTA 225 (chr 15: 729,830)	G → C (Trp → Cys)	Illumina: 1% (2/201)* Sanger: NA	Illumina: 79% (88/112) Sanger: 50% (5/10)	Illumina: 84% (123/146) Sanger: NA	Illumina: 79% (94/119) Sanger: NA	Illumina: 23% (39/166) Sanger: NA	Illumina: NA Sanger: 30% (3/10)	Illumina: 44% (40/91) Sanger: NA
	rtTA 329 (chr 15: 729,934)	A → C (Tyr → Ser)	Illumina: 3% (6/215)* Sanger: NA	Illumina: 5% (6/112) Sanger: 10% (1/10)	Illumina: 3% (4/143)* Sanger: NA	Illumina: 3% (4/152) Sanger: NA	Illumina: 0% Sanger: NA	Illumina: NA Sanger: 0%	Illumina: 0% Sanger: NA
	rtTA 431 (chr 15: 730,036)	G → T (Cys → Phe)	Illumina: 2% (3/182)* Sanger: NA	Illumina: 6% (6/101) Sanger: 0%	Illumina: 1% (2/159)* Sanger: NA	Illumina: 1% (2/145)* Sanger: NA	Illumina: 1% (2/162)* Sanger: NA	Illumina: NA Sanger: 0%	Illumina: 0% Sanger: NA
24hr, r2	rtTA 225 (chr 15: 729,830)	G → C (Trp → Cys)							Illumina: 53% (60/113) Sanger: NA
	rtTA 225 (chr 15: 729,830)	G → T (Trp → Cys)							Illumina: 42% (47/113) Sanger: NA
24hr, r3	rtTA 728 (chr 15: 730,333)	T → A (Leu → stop)							Illumina: 96% (68/71) Sanger: NA

Appendix Table S5. Mutations detected by whole-genome Illumina sequencing and targeted Sanger sequencing in conditions DiZ2 and D2Z2 (both antibiotic and inducer).

(A) Mutations in condition DiZ2. All columns are as indicated for ***Appendix Table S2****.*

(B) Mutations in condition D2Z2. All columns are as indicated for ***Appendix Table S2****.*

Appendix Figure S1

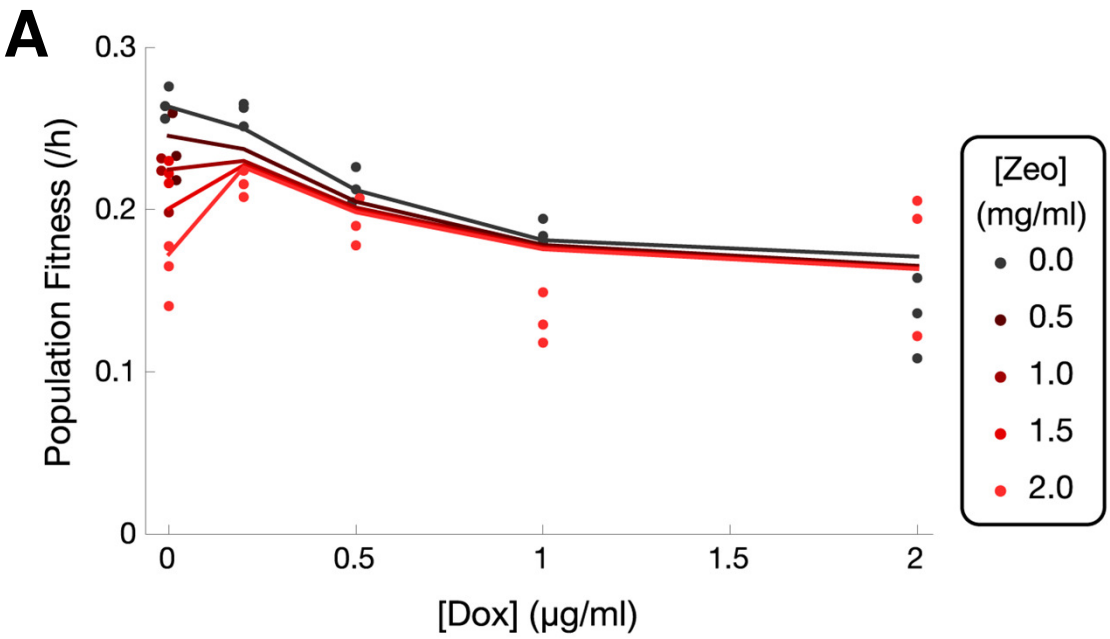

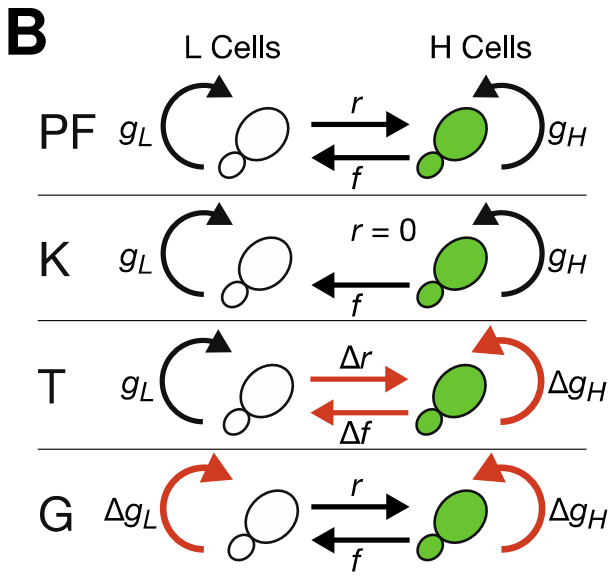

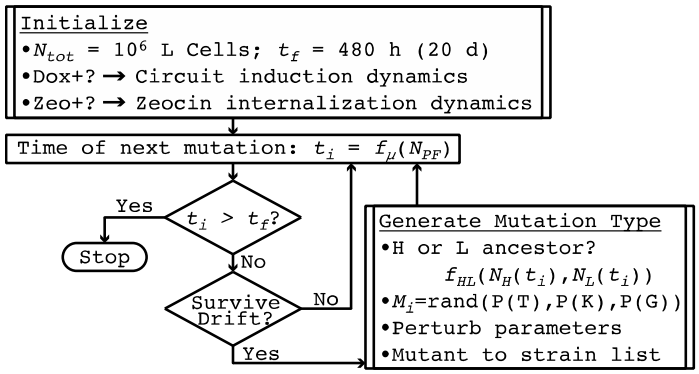

App. Fig. S2

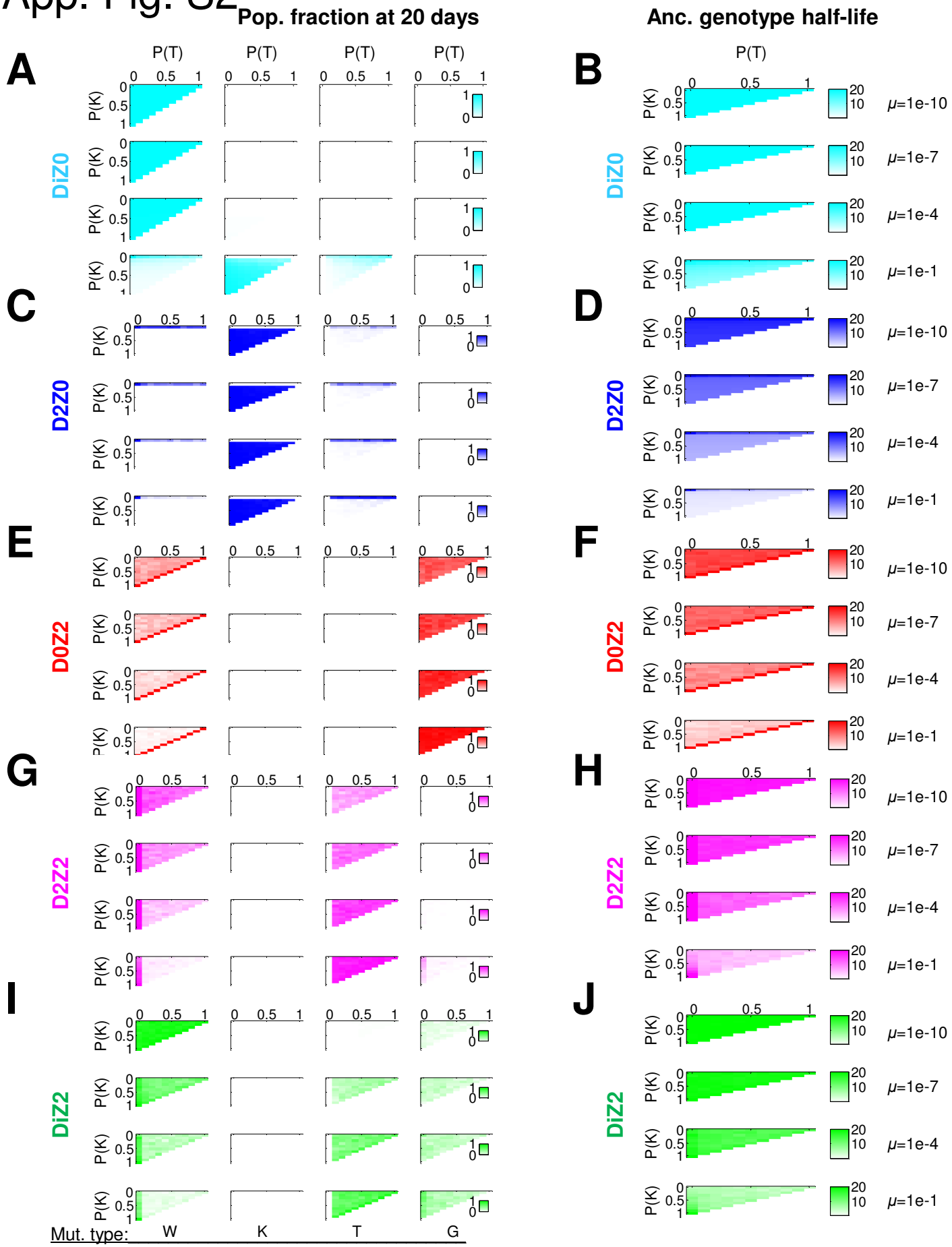
Pop. fraction at 20 days
Anc. genotype half-life
A
B
C
D
E
F
G
H
I
J
DiZ0
D2Z0
D0Z2
D2Z2
DiZ2
P(T)
P(K)
μ=1e-10
μ=1e-7
μ=1e-4
μ=1e-1
Mut. type:
W
K
T
G

Appendix Figure S3

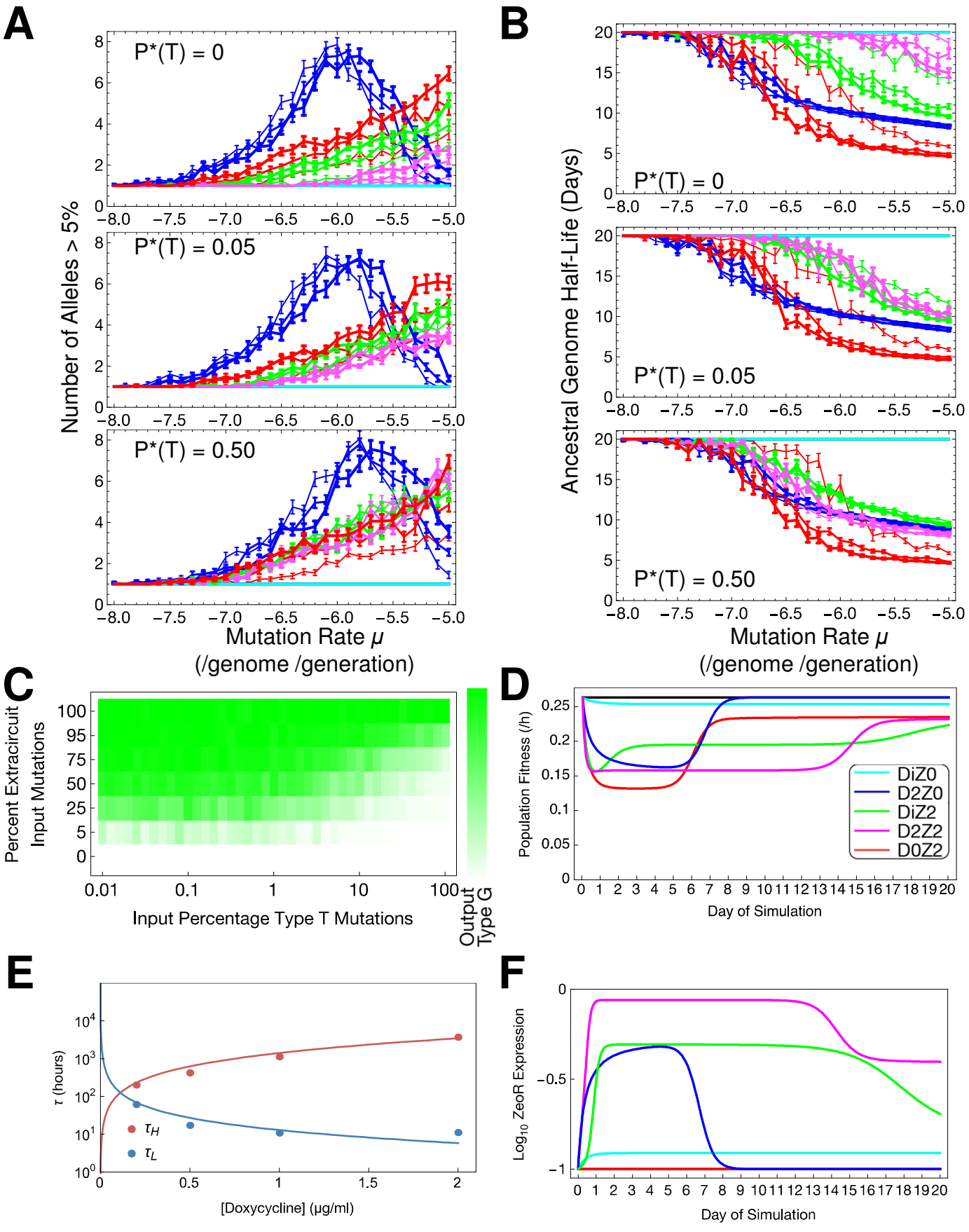

Appendix Figure S4

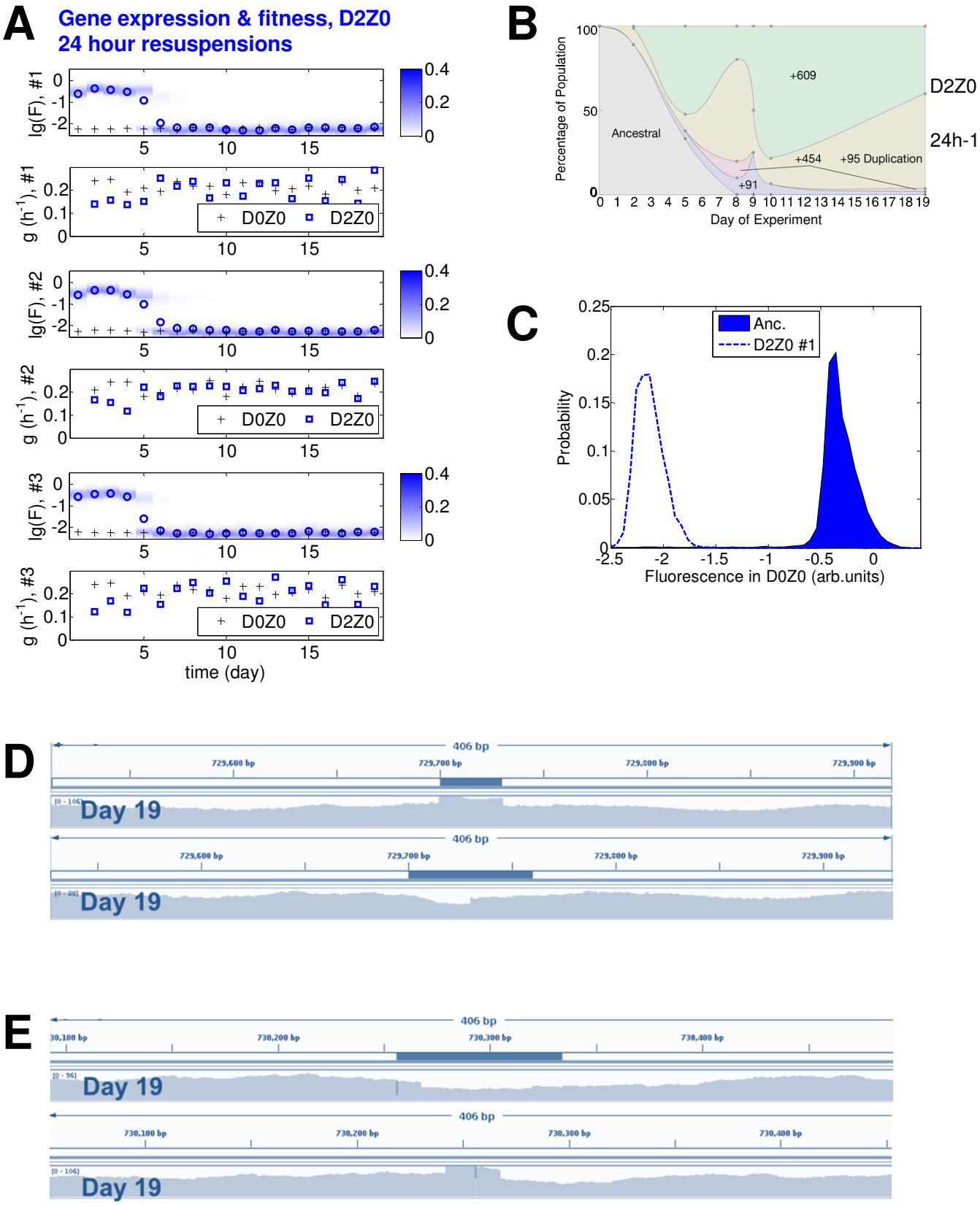

Appendix Figure S5

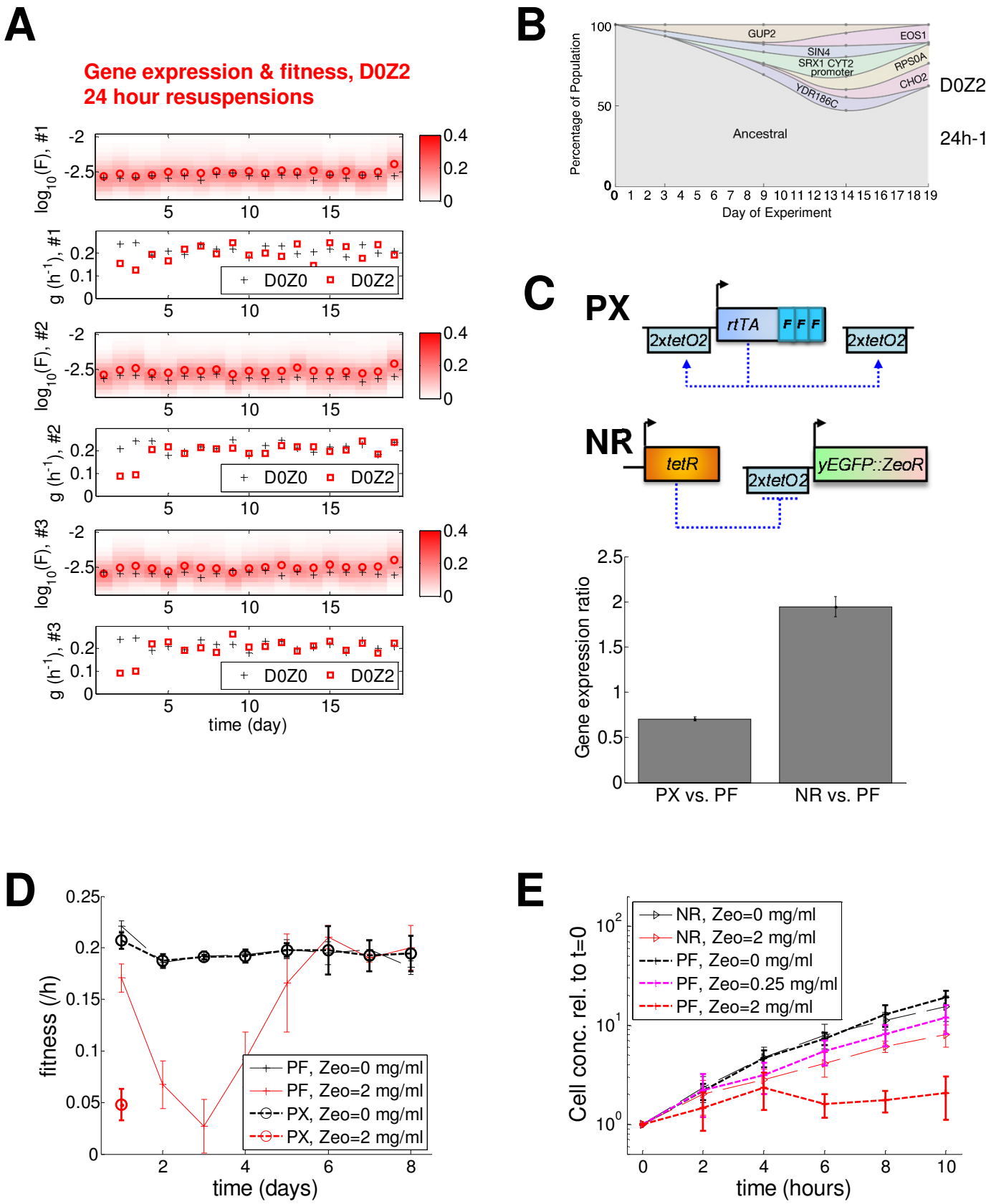

Appendix Figure S6

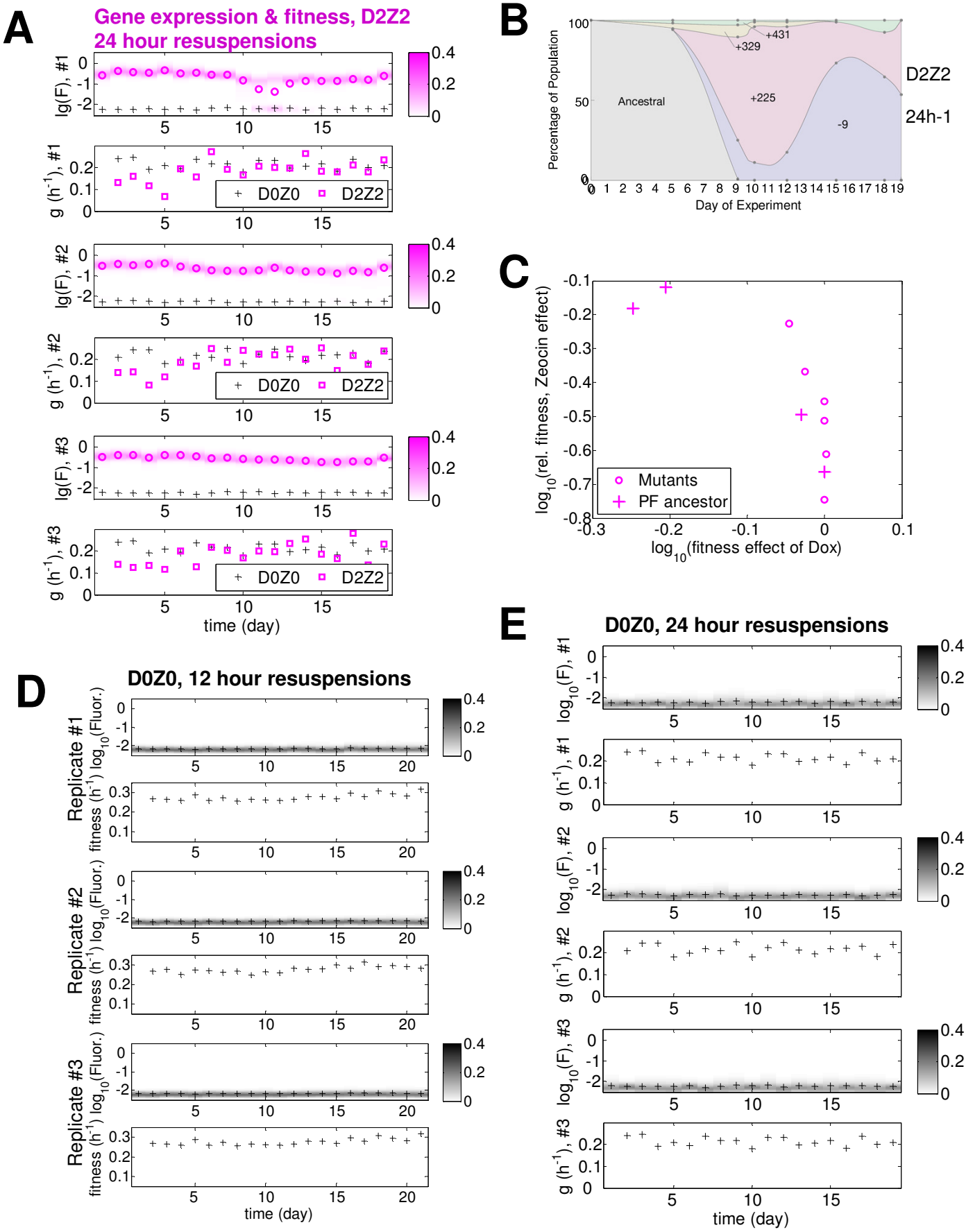

Appendix Figure S7

A

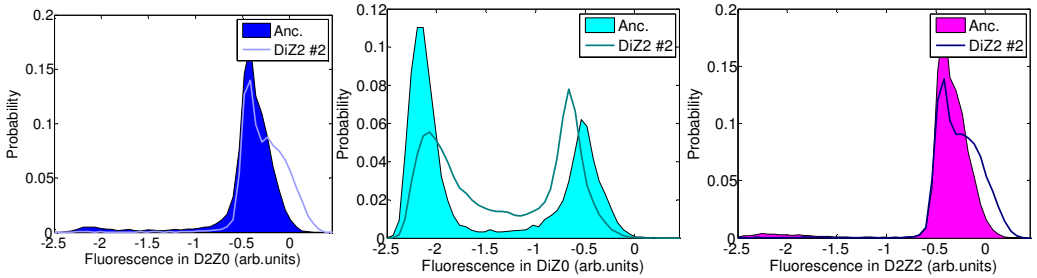

B

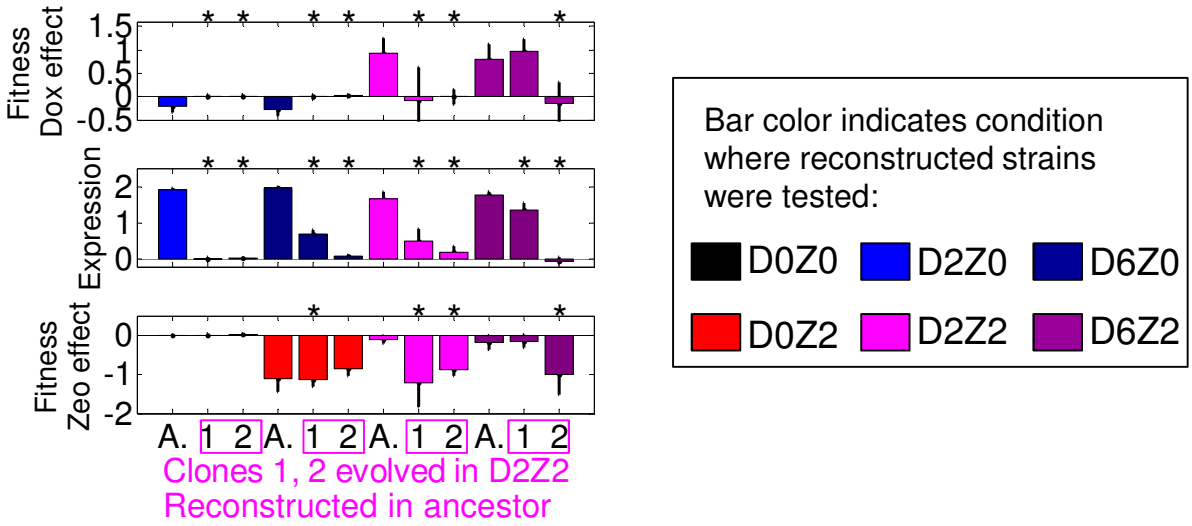

C

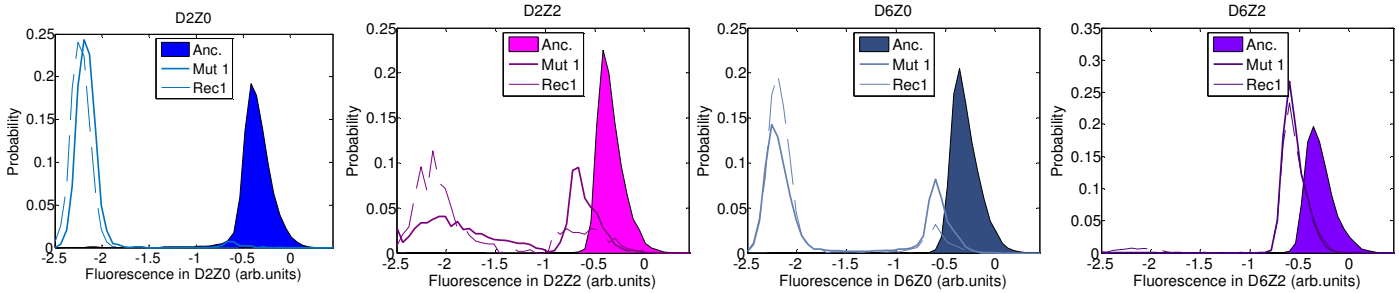

D

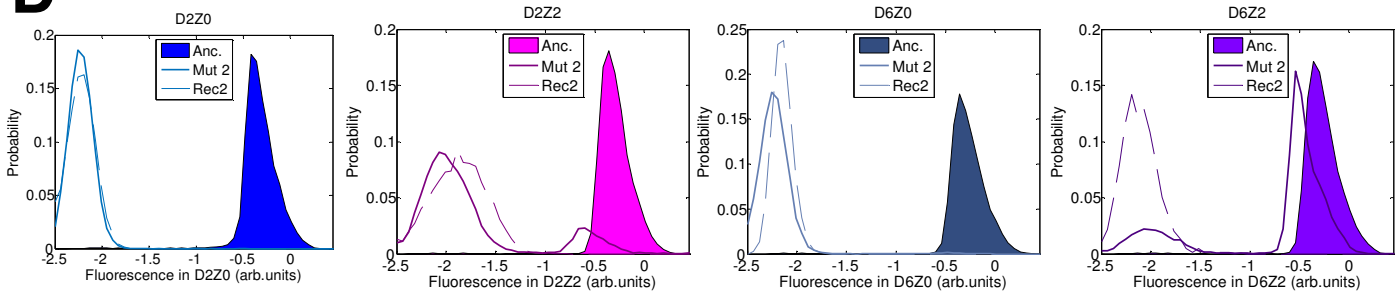

Appendix Figure S8